



Originally published as:

Rybacki, E., Meier, T., Dresen, G. (2016): What controls the mechanical properties of shale rocks? – Part II: Brittleness. - *Journal of Petroleum Science and Engineering*, 144, pp. 39–58.

DOI: <http://doi.org/10.1016/j.petrol.2016.02.022>

What controls the mechanical properties of shale rocks? – Part II: Brittleness

E. Rybacki, T. Meier, G. Dresen

uddi@gfz-potsdam.de

Abstract

Successful stimulation of shale gas reservoirs by hydraulic fracturing operations requires prospective rocks characterized by high brittleness to prevent fast healing of natural and hydraulically induced fractures and to decrease the breakdown pressure required to (re-) initiate a fracture. We briefly reviewed existing brittleness indices (B) and applied several, partly redefined, definitions relying on composition and deformation behavior on various, mainly European black shales with different mineralogical composition, porosity and maturity. Samples were experimentally deformed at ambient and elevated pressures (P) and temperatures (T), revealing a transition from brittle to semibrittle deformation behavior with increasing pressure and temperature. At given composition and deformation conditions, B values obtained from different definitions vary considerably. The change of B with applied deformation conditions are reasonably well captured by most definitions based on the stress-strain behavior, which do not correlate with the fraction of individual phases, e.g., clay content. However, at given deformation conditions, most composition-based indices show similar variations with bulk composition as those derived from stress-strain behavior. At low P - T conditions ($\lesssim 4$ km depth), where samples showed pronounced post-failure weakening, B values determined from composition correlate with those calculated from pre-failure stress-strain behavior and both correlate with the static Young's modulus. In this regime, the brittleness concept can help to constrain successful hydraulic fracturing campaigns and brittleness maybe estimated from core or sonic logs at shallow depth. However, long term

p [1]

creep experiments are required to estimate in-situ stress anisotropy and the healing behavior of hydraulically induced fractures.

Keywords

shale, brittleness, strength, fracability, unconventional reservoirs

1. Introduction

In the past decades, the increasing fossil energy demand pushed the exploitation of unconventional hydrocarbon reservoirs, in particular oil and gas shales. Multi-stage hydraulic fracturing stimulations are common practice to enhance the production rate. Successful fracturing campaigns in prospective shale plays with low proppant embedment aim at maximizing the stimulated rock volume (e.g., Wang and Gale, 2009; Berard et al., 2012). Efficient stimulation of the reservoir requires a good knowledge of the rock mechanical properties.

The mechanical behavior of shales may be classified into brittle and ductile (e.g., Nygard et al., 2006; Jaeger et al., 2007; Fjaer et al., 2008; Holt et al., 2011). Brittle shales are expected to contain natural fractures and are more easily fractured by hydraulic stimulation. In contrast, ductile shales are believed to show fast fracture healing and to pose constraints on the mud weight window in order to avoid borehole breakouts (e.g., Rickman et al., 2008; Holt et al., 2011; Mullen and Enderlin, 2012). In petroleum engineering, this distinction in the mechanical response of source rocks is commonly described in terms of rock brittleness or fracability (e.g., Holt et al., 2011, 2015; Yang et al., 2013; Jin et al., 2014), sometimes also termed fragility, penetrability, drillability, or cuttability in mining sciences (e.g., Thuro and

Spaun, 1996; Altindag, 2002; Kahraman and Altindag, 2004; Tiryaki, 2006). The opposite behavior is usually denoted as ductility. Unfortunately, no unique definition of brittleness exists and many different index definitions have been proposed to quantify the degree of brittle or ductile deformation behavior (e.g., Hucka and Das, 1974; Andreev, 1995; Holt et al., 2011, 2015; Yang et al., 2013; Jin et al., 2014). According to Andreev (1995), brittleness can be regarded as a material property, where brittle rocks have high mechanical strength and the deformation/failure behavior displays a low degree of inelasticity and strong localization. This is in contrast to ductile deformation, which is non-localized on a macroscopic scale. The prevailing deformation mechanisms (i.e., microcracking vs. intracrystalline plasticity) result in a scale dependent mechanical behavior. A rock may respond to mechanical loading brittle on a (grain) microscale, but ductile on a macroscopic (sample) scale (Rutter, 1986). The (ductile) transitional regime between brittle and plastic deformation is called semibrittle (Evans et al, 1990, Evans and Kohlstedt, 1995). Therefore, brittleness depend not only on material properties, like composition, porosity, water content, structure and texture, but also on boundary conditions, as for example loading rate, temperature, effective differential stress and confining pressure.

Because of this complexity, the determination of brittleness of specific shale requires advanced laboratory testing procedures, which are time-consuming and relatively expensive. Accordingly, other empirical definitions of brittleness were proposed that are more easily estimated from borehole or mud logging. These are based on dynamic elastic parameters (Young's moduls and Poisson's ratio, e.g., Grieser and Bray, 2007; Rickman et al., 2008) or composition (fraction of strong versus weak minerals, e.g., Jarvie et al., 2007; Wang and Gale, 2009), respectively.

We deformed (mainly European) black shales with different composition, maturity and porosity at varying confining pressures, temperatures and deformation rates. The results are

described in an accompanying paper (Rybacki et al., 2015) showing that, at preset pressure-temperature conditions, the strength and Young's modulus can be estimated roughly from the volumetric fraction of strong minerals (quartz, feldspar, pyrite), carbonates (intermediate strong fraction in shales), weak constituents (clay, kerogen) and pores. However, at given composition and porosity, the mechanical response and associated brittleness depend on the external conditions (pressure, temperature), which may not be captured by most common brittleness index definitions. Here, we examine the brittleness of shales with varying composition and porosity in response to the applied deformation conditions.

2. Sample Materials and Experimental Methods

The examined black shales comprise 4 different immature to overmature Posidonia shales (Dotternhausen = DOT, Wickensen = WIC, Harderode = HAR and Haddessen = HAD) from Germany and overmature Alum (= ALM) shale from the island of Bornholm (Denmark). In addition, we inspected mature Barnett (=BAR) shale from Texas (USA) and reference samples composed of the main constituents of shales (NOV = Arkansas novaculite, GRA = Westerly granite, GAB = Panzhihua gabbro, FST = Flechtingen sandstone, BST = Bentheim sandstone, LIM = Solnhofen limestone, MAR = Carrara marble, COA = black coal). The shale maturity, described by Vitrinite reflectance, varies between 0.6 and 3.6 VRr% and the porosity between 0.6 and 11 vol%, measured by mercury intrusion porosimetry (MIP). Note that the total connected porosity, estimated from He-pycnometry, is usually 1-2 vol% higher compared to MIP values, but for Alum shale up to 8 vol% higher. The shale composition, determined by X-ray diffraction analysis (XRD), is quite variable with 17-62 vol% clay (illite, illite-smectite, kaolinite), 0-50 vol% carbonates, 7-46 vol% quartz, 0-10 vol% feldspar, and 0-7 vol% pyrite. The total organic carbon content (TOC) is 2-22 vol%. Most Alum samples are poor in carbonates with a high amount (\approx 60-70 vol%) of mechanically weak components

p [4]

(clay, kerogen) and about 30-40 vol% strong minerals (quartz, feldspar, pyrite). In contrast, Posidonia shales contain a high fraction of carbonates ($\approx 25-45$ vol%), $\approx 40-60$ vol% weak and $\approx 10-20$ vol% strong phases, whereas Barnett shale consists of ≈ 10 vol% carbonate, $\approx 40-50$ vol % weak and $\approx 30-50$ vol% strong components (Fig. 1). The composition of the reference samples and some specific shale samples used for triaxial compression are given in Tab. 1.

The transverse isotropic shale samples contain distinct bedding planes that are rich in organic matter with subparallel oriented pyrite flakes and calcareous bands. The grain size is typically < 5 μm . A more detailed description of the composition and microstructures is given by (Rybacki et al., 2015). The water content of Posidonia and Barnett shale was $\approx 1-2$ wt% and of Alum shale ≈ 4 wt%, determined by drying of samples until zero weight loss. For axial compression experiments, cylindrical samples were prepared with dimensions of 50 mm length and 25 mm diameter or 20 mm length and 10 mm diameter for tests at room and elevated temperatures, respectively. Brazilian disc tests were performed on samples of 30 mm diameter and > 15 mm length.

Most tests at ambient temperature were performed at constant deformation rates of 0.2 mm/min using a stiff, servo-hydraulically controlled deformation apparatus (MTS). The tensile strength, σ_T , was determined from Brazilian disc tests in accordance with the ISRM suggested method (Bieniawski and Hawkes, 1978). The uniaxial compressive strength, σ_C , and associated strain were determined from the recorded load displacement data, corrected for the system stiffness. Triaxial strength (peak stress), σ_{max} , values were measured at (oil) confining pressures, P , between 17.5 and 70 MPa, using rubber-jackets for sealing. Triaxial deformation experiments at elevated temperature were performed in a Paterson-type deformation apparatus (Paterson, 1970) at constant strain (deformation) rates, using argon gas as confining pressure medium. Measured forces were corrected for the strength of copper

p [5]

sleeves used to jacket the samples and converted to axial stress assuming constant volume deformation. Axial displacements were corrected for the system compliance. The estimated error of stress and strain values is < 4%. Because of the low stiffness of the Paterson apparatus and using copper as jacket material, the Young's modulus and post-failure deformation behavior measured at elevated temperature is less accurate with an estimated error < 20%.

3. Quantification of Brittleness

Various suggested brittleness indices are summarized in the appendix, yielding more than 36 different definitions that are empirical and based on different parameters. Here, we used selected brittleness indices related to sample composition (Tab. A1), to the mechanical deformation behavior (Tab. A2) and to elastic properties (Tab. A3), most of which are accessible from our measurements. We do not include indices that rely on indentation testing (Tab. A4) and various other definitions related to core diskling, crushing, overconsolidation ratios and others (Tab. A5). We evaluated the following 12 indices.

Brittleness indices based on rock composition, relating the fraction of strong/brittle minerals (numerator in Eqns. 1-3) to the fraction of strong/brittle and weak/ductile components (denominator, cf., Eqn. A1). The following definitions were tested:

$$B_{comp01} = \frac{F_{Qtz}}{F_{Qtz} + F_{Cb+Clly}}, \quad (1)$$

$$B_{comp02} = \frac{F_{Qtz+Dol}}{F_{Qtz+Dol} + F_{Cal+Clly+TOC}}, \quad (2)$$

$$B_{comp03} = \frac{F_{Qtz+Cb}}{F_{Qtz+Cb} + F_{Clly+TOC}}, \quad (3)$$

proposed by Jarvie et al. (2007), Wang and Gale (2009), and Glorioso and Rattia (2012), respectively, where $B_{compo} = 1$ indicates brittle and $B_{compo} = 0$ ductile rocks. We did not include the definition by Jin et al. (2014), which is quite similar criterion to B_{compo3} and considers feldspar, but also mica as strong and brittle minerals (cf. Eqn. A1). Mineral abbreviations are Qtz = quartz, Cb = carbonate, Cly = clay, Dol = dolomite, Cal = calcite. All fractions F are given in wt%. Here, we use for determination of B_{compo} volume fractions instead of weight fractions, because from the mechanical point of view the volume fraction and distribution of the various minerals may determine the capacity to build up a load-bearing framework and to support or redistribute applied stresses. For the investigated shales, the difference in fractions of minerals given in vol% or wt% is up to about 8%, mainly affected by porosity and the low TOC density as well as high pyrite (Py) density compared to the other minerals.

In addition, we propose a modified brittleness criterion for shales, since under most in-situ conditions the strength of shale constituents can be roughly divided into mechanically strong = Qtz + Fsp + Py = QFP, mechanically intermediate strong = Cb, and mechanically weak = Cly + TOC = ClyTOC components (Rybacki et al., 2015, cf., Fig. 1). Fsp denotes feldspar. Because also porosity, Φ , affects the strength, the suggested index is (cf., Eqn. A2):

$$B_{porocomp} = \frac{w_{QFP} F_{QFP}}{w_{QFP} F_{QFP} + w_{Cb} F_{Cb} + w_{ClyTOC} F_{ClyTOC} + w_{\phi} \phi}, \quad (4)$$

where w_{QFP} , w_{Cb} , w_{ClyTOC} , and w_{ϕ} are weighting factors that range between 0 and 1 and may be adapted to deformation conditions. Here, we set $w_{QFP} = w_{ClyTOC} = w_{\phi} = 1$ and $w_{Cb} = 0.5$ based on the strength contrast (Rybacki et al., 2015, see also below).

From the set of brittleness definitions related to elastic properties (Tab. A3), we used a simplified version of Eqn. (A17) that neglects the influence of Poisson's ratio (cf., Grieser and Bray, 2007):

$$B_{Young} = \frac{E - E_{min}}{E_{max} - E_{min}} \quad (5).$$

Here, we adopted the lower limit of $E_{min} = 0$ GPa suggested by Grieser and Bray (2007) and set $E_{max} = 83$ GPa based on the Young's modulus of novaculite measured at ambient conditions (cf., Rybacki et al., 2015). We did not use the limits ($E_{min} = 7$ GPa, $E_{max} = 55$ GPa) suggested by Rickman et al. (2008), because they are presumably based on the prospectivity of Barnett shale. Unfortunately, for most shales no clear initial linear (-elastic) slope of the stress-strain curve and associated yield point could be identified, which did not allow easy determination of the elastic strain. Therefore, we defined the static Young's modulus by the 50%-secant modulus, determined from the slope of stress-strain curves from the origin to the strain measured at 50% of the peak stress (Fig. 2). For comparison, the tangent modulus measured at $\approx 50\%$ of the peak stress typically resulted in 20-30% lower Young's moduli.

The other brittleness indices presented here are based on the mechanical deformation behavior of rocks (see, for example, reviews by Hucka and Das, 1974; Andreev, 1995; Holt et al., 2011; Tasarov and Potvin, 2013, Jin et al., 2014). At ambient pressure and temperature, brittleness was defined by the ratio of compressive uniaxial strength σ_C and tensile strength σ_T (Hucka and Das, 1974, cf., Eqn. A9):

$$B_{tensile} = \frac{\sigma_C - \sigma_T}{\sigma_C + \sigma_T} \quad , \quad (6)$$

yielding $B_{tensile} = 1$ if $\sigma_C \gg \sigma_T$ (brittle) and $B_{tensile} = 0$ (ductile) for $\sigma_C = \sigma_T$. By definition, this criterion cannot account for the influence of pressure and temperature on brittleness. An alternative index is based on the product of σ_C and σ_T (Altindag, 2002, cf. Eqn. A10), but as

pointed out by Denkhaus (2003 a, b), this definition does not capture the observation that the ratio of compressive to tensile strength increases with increasing brittleness and is therefore not considered here.

The remaining criteria refer to the stress-strain behavior in (tri-) axial compression. A typical deformation curve for shales is shown in Fig.2, which reveals continuous non-linear hardening up to the peak stress σ_{max} and associated peak strain ε_{max} that may coincide with the failure stress σ_{fail} and strain ε_{fail} if the rock is entirely brittle. Macroscopic failure usually occurs at slightly higher strain than ε_{max} , particularly for semibrittle behavior, where both brittle and plastic deformation mechanisms interact. Here, we used the maximum stress and strain as failure conditions, because the onset of failure was hard to identify, at least for tests performed in the Paterson apparatus. Brittleness may be then defined by the pressure sensitivity of the rock strength, expressed by the coefficient of internal friction μ in the Mohr-Coulomb failure criterion (Hucka and Das, 1974, cf., Eqn. A8):

$$B_{Mohr} = \mu / \sqrt{1 + \mu^2} \quad (7).$$

Clay-rich rocks may yield a very low friction coefficient (≈ 0.1), resulting in a low brittleness index value (≈ 0.1), whereas strong and clastic rocks may have rather high μ values (up to ≈ 0.9 , yielding $B_{Mohr} \approx 0.7$).

From the (pre-) failure region of stress-strain curves, brittleness can be also defined by the ratio of elastic (subscript *el*) to maximum or failure (subscript *fail*) strain ε (see Hucka and Das, 1974; Andreev, 1995, cf., Eqn. A3):

$$B_{preStrain} = \frac{\varepsilon_{el}}{\varepsilon_{fail}} = \frac{\varepsilon_{el}}{\varepsilon_{el} + \varepsilon_{inel}} \quad (8),$$

or by the corresponding ratio of energies W (cf., Eqn. A4):

$$B_{preWork} = \frac{W_{el}}{W_{fail}} = \frac{W_{el}}{W_{el} + W_{inel}}, \quad (9)$$

where $B = 1$ (brittle) if the rock is fully elastic until failure and $B \rightarrow 0$ (ductile) if inelastic deformation (subscript *inel*) is predominant (Fig. 2). Brittleness may be also quantified using the fracture initiation point instead of the elastic limit (Fig. 2, cf., Eqns. A6, A7), commonly associated with the onset of dilatancy constrained from volumetric strain measurements. In compact rocks, the onset of frac initiation may coincide with the yield point given by the origin of non-linearity in the stress-strain curve.

As a simplified version of Eqn. (9), we suggest quantifying brittleness by taking into account the hardening behavior by calculating the ratio of the (linearized) hardening modulus H to the Young's modulus E (Fig. 2, cf., Eqn. A5):

$$B_{preHarden} = \frac{H}{E} = \frac{\sigma_{inel}}{\varepsilon_{inel}} \frac{1}{E} = \frac{\sigma_{fail} - \sigma_{el}}{\varepsilon_{fail} - \varepsilon_{el}} \frac{1}{E} \quad (10).$$

Again, $B_{preHarden} = 1$ for brittle (pure elastic) deformation and $B_{preHarden} \rightarrow 0$ for elasto-plastic behavior.

From the post-failure based definitions (Tab. A2) we adopted two brittleness indices related to the post failure stress and strain. Unfortunately, most deformed shales did not show a well-defined or constant residual (friction) strength, which was either related to semibrittle behavior or to technical issues in the Paterson apparatus. Therefore, these approaches strongly depend on the appropriate selection of post failure data and on the machine stiffness. In cases of gradual weakening with no well-defined residual strength, we used for the determination of the residual strain and associated strength the intersection between the descendant modulus M and the approximate linear slope slope at the end of the stress-strain curve close to the

expected plateau (Fig. 2). Smolczyk and Gartung (1979) defined brittleness by the ratio of the post-failure stress drop to the maximum or failure stress (Fig.2, cf., Eqn. A11):

$$B_{resStress} = \frac{\sigma_{fail} - \sigma_{res}}{\sigma_{fail}}, \quad (11)$$

where σ_{res} is the residual (friction) strength, which yields brittle behavior for $\sigma_{res} = 0$ ($B_{resStress} = 1$) and plastic behavior for $\sigma_{res} = \sigma_{fail}$ ($B_{res} \rightarrow 0$). In terms of residual strain, ε_{res} , a modified definition of Eqn. (A13) gives:

$$B_{resStrain} = \frac{\varepsilon_{fail}}{\varepsilon_{res}}, \quad (12)$$

which varies again between 1 (brittle) if $\varepsilon_{res} = \varepsilon_{fail}$ and 0 (ductile) if $\varepsilon_{res} \gg \varepsilon_{fail}$. Here, we did not consider the ‘intrinsic’ brittleness definitions (Eqns. A15, A16) and the combined index (Eqn. A12) because of their strong sensitivity to machine stiffness.

4. Results

We performed 54 triaxial compression tests on small samples normal to bedding in the Paterson apparatus at confining pressures of 50-400 MPa, temperatures between 20 and 400°C, and axial strain rates of 5×10^{-3} - 5×10^{-7} s⁻¹. In addition, 24 tests on large samples were performed in the MTS apparatus at room temperature, axial strain rate of $\approx 7 \times 10^{-5}$ s⁻¹ and confining pressures between 15.5 and 75 MPa, as well as 34 uniaxial compression tests and 60 Brazilian disc tests. Large samples were loaded normal and parallel to bedding. Since a number of measurements were achieved on samples from almost similar depth, here we report only the corresponding average values.

The basic mechanical results in terms of strength and static Young's modulus in relation to composition, porosity, bedding orientation, water content and applied deformation conditions (pressure, temperature, strain rate) are described in detail by Rybacki et al. (2015). In the following, we first show some representative stress-strain curves and secondly the associated brittleness values calculated from Eqns. 1 - 12.

4.1 Stress-strain behavior

The influence of deformation conditions on the stress-strain behavior for immature, Cb-rich Posidonia shales (Dotternhausen and Wickensen) and overmature, Cly-rich Alum shale is shown in Fig. 3. Typical for brittle deformation, the strength increases with increasing confining pressure, but the shape of stress-strain curves also changes gradually from post-peak strain weakening at low confinement to steady state deformation at high pressure, indicating ductile behavior (Fig. 3a). In accordance with this transition in the shape of curves, a transition of the macroscopic deformation behavior occurred from single shear fractures at low P to homogeneous barreling without distinct fractures at high P . On the microscale, deformation is associated with microcracking of strong particles, shearing and bending of weak components, indentation of strong into weak phases and pore collapse at low pressure (Rybacki et al., 2015). Applying a Mohr-Coulomb failure criterion, the coefficient of internal friction decreases non-linearly with increasing pressure approaching $\mu = 0.18$ at $P > 50$ MPa. The friction coefficient of the other Posidonia shales is comparable (0.21 - 0.34), whereas for Alum shale $\mu = 0.36 - 0.55$ and for Barnett $\mu = 1.08$ (Rybacki et al., 2015).

Increasing temperature up to about 75°C - 100°C yields no significant change of strength of DOT samples. At higher temperatures between 100 and 400°C, strength decreases continuously, associated with a small increase of peak strain (Fig. 3b). At the applied pressure

of 50 MPa, all samples failed along a single fracture except at 400°C. Here, the sample showed a broad shear zone, associated with the onset of kerogen decomposition and pyrolysis. The observed temperature dependence of strength is typical for thermally activated deformation mechanisms such as dislocation glide of clay minerals (e.g., Rybacki et al., 2015). On the other hand, reducing the strain rate by > 4 orders of magnitude decreases the peak stress of WIC samples by less than 17% combined with slightly increased post-failure weakening (Fig. 3c). In contrast, water has a very strong influence on the strength (Fig. 3d), where dry Alum samples with ≈ 0.01 wt% H₂O are considerably stronger than water saturated samples (≈ 3.8 wt% H₂O). Also, the loading direction with respect to bedding affects the strength and Young's modulus, reflecting the transvers isotropic properties of shales (Fig. 3d). The influence of composition on the stress-strain behavior at fixed strain rate is shown in Fig. 4 for uniaxial and triaxial compression tests at temperatures between 20° and 200°C and confining pressures of 0.1, 50 and 100 MPa. At ambient conditions, most samples show minor inelastic deformation before peak stress and small stress drops in the post peak regime before failure occurred (Fig. 4a). Carbonate-rich Posidonia samples appear to be stronger than the clay-rich Alum and Barnett samples. With increasing pressure and temperature, the post peak strain weakening reduces (Fig. 4 b-d) and the macroscopic failure behavior often changes from localized faulting to barreling. Most Posidonia samples exhibit a smooth post-failure weakening at high P - T conditions, except the low porosity HAR sample and BAR and ALM shales, although the compositions of the latter are quite different (Fig. 1). Note that the post peak strain weakening gradient at elevated pressure is likely smoothed by the strength of the Cu jacket material and the electro-mechanical servo-control of the Paterson deformation apparatus.

The stress-strain curves of the reference samples deformed at $P = 50$ MPa and $T = 100^\circ\text{C}$ are shown in Fig. 4e. The mineral content of these samples reflect the main constituents of shales

(Tab. 1). Samples composed of strong minerals (QFP) are brittle displaying elastic deformation up to peak stress and failure that occurred at very high stress (≈ 700 MPa, Fig. 4 e). For comparison, Flechtingen and Bentheim sandstones have lower strength (≈ 200 - 300 MPa) due to the high porosity of ≈ 9 and 24% , respectively. The tested carbonate rocks range between ≈ 320 MPa for LIM and 230 MPa for MAR, whereas black coal is the weakest material (≈ 150 MPa). The marble and coal show ductile stress-strain behavior reaching almost steady state deformation. Deformed samples were barrel-shaped with abundant microcracks after deformation. Coal samples may be regarded as a proxy for the strength of pure kerogen. However, the strength of biotite/clay (≈ 90 MPa) is a better estimate for the strength of weak phases in shales than the strength of coal (Rybacki et al., 2015).

4.2 Brittleness index values

The brittleness (B) values calculated from Eqns. 1- 12 vary substantially between 0.01 and 1.0 (Tabs. 2, 3), depending on definition, rock type, and deformation conditions. Typical examples of the variation of deformation behavior-based indices (Eqns. 8-12) for WIC and HAR shales deformed between $P = 0.1$ MPa, $T = 20^\circ\text{C}$ and $P = 100$ MPa, $T = 200^\circ\text{C}$ (cf., Fig. 4) are shown in Figs. 5a and b, respectively. Almost all indices show the highest brittleness at ambient conditions and decreasing B values (higher ductility) with increasing pressure and temperature. Absolute values strongly depend on definition with highest values determined from strain (Eqn. 8 = $B_{preStrain}$, Eqn. 12 = $B_{resStrain}$). In comparison, brittleness estimated from normalized Young's modulus (Eqn. 5 = B_{Young}) varies hardly with applied conditions, but slightly decreases at high temperature (Fig. 5, Tab. 2).

The variation of brittleness values of shales determined from stress-strain curves measured at varying pressures, temperatures, strain rates and water content (cf., Fig. 3) are shown in Fig.

6. Because of the similar trends of deformation behavior-based indices with varying conditions (Fig. 5), in the following we just use $B_{preWork}$ (Eqn. 9) and $B_{resStress}$ (Eqn. 11) for (pre-) and post failure-based definitions, respectively, in conjunction with B_{Young} . At $T = 20^{\circ}\text{C}$, Dotterhausen shale shows decreasing $B_{preWork}$ values with increasing pressure up to $P \approx 150$ MPa (Fig. 6a), where almost steady state deformation is achieved (cf., Fig. 3a). A similar trend is derived using $B_{resStress}$ exception at ambient pressure. In contrast, B_{Young} is almost unaffected by pressure. The temperature sensitivity of deformation behavior-based brittleness indices, measured on DOT samples at $P = 50$ MPa, is relatively low with a slight decrease up to 300°C and a strong increase at 400°C except for $B_{resStress}$ (Fig. 6b, Tab. 3). Also B_{Young} decreases slightly with increasing T . There is no clear effect of strain rate on the brittleness of WIC samples deformed at $T = 100^{\circ}\text{C}$ and $P = 50$ MPa. Usually, decreasing strain rate is expected to facilitate plastic deformation processes, which yields decreasing peak stresses, but here also stronger post failure weakening. The influence of water saturation on brittleness is low if samples were dried, determined for Alum samples at $T = 100^{\circ}\text{C}$ and $P = 50$ MPa (Fig. 6d). For water saturated samples, however, pre-failure based B index indicates an increase of brittleness, whereas the post-failure definition suggests higher ductility.

A comparison of B values of shales and reference samples determined at $T = 100^{\circ}$, $P = 50$ MPa is shown in Fig. 7a. At these conditions, BAR and to some extent also ALM and HAR shales show the largest values of $B_{preWork}$ and B_{Young} , whereas DOT, WIC and HAD are relatively ductile, in agreement with the stress-strain curves (Fig. 4c). $B_{resStress}$ shows somewhat different results with ALM as most ductile and BAR and DOT as most brittle rocks. Concerning the brittleness of the reference samples, $B_{preWork}$ predicts brittle behavior of samples with a high fraction of strong minerals and low porosity (novaculite, granite), intermediate values for the high porosity sandstones and low values for carbonates and coal. $B_{resStress}$ shows similar trends except for granite and limestone with intermediate values. B_{Young}

also predicts comparable values to $B_{preWork}$, but a relatively high brittleness of carbonates (Fig. 7a). In general, B values for different Posidonia shales become more similar at elevated P - T conditions (Tab. 2). In comparison, at ambient pressure and temperature all deformation behavior-based indices indicate relatively brittle behavior, except $B_{resStress}$ and B_{Young} , which indicate mostly ductile behavior (Tab. 2).

Estimating brittleness from frictional strength (Eqn. 7 = B_{Mohr}) yields relatively high values for carbonates, sandstone and granite, comparable to those of ALM and BAR shales (Fig. 7b). In contrast, Posidonia shales are more ductile with slightly decreasing index values with increasing temperature, comparable to the effect of bedding orientation. In comparison, B_{Mohr} of WIC shale is higher than of the other Posidonia shales, whereas $B_{preWork}$, $B_{resStress}$ and B_{Young} are highest for HAR shale (Fig. 7a). Brittleness estimated from tensile and unconfined compressive strength (Eqn. 6 = $B_{tensile}$) yield quite high values of $\approx 0.7 - 0.9$ for almost all rocks (Fig. 7c), independent of bedding orientation. These estimates fit only to the mechanical behavior of shales at ambient conditions (Fig. 4a).

Brittleness values calculated from composition (Eqns. 1-3, 4 = $B_{compo1-3}$, $B_{porocomp}$) are shown in Fig. 7d. For shales, they show a similar trend with values between about 0.1 and 0.4. For Posidonia samples, the highest values as obtained for HAR shale, similar to $B_{preWork}$ and B_{Young} . However, B_{compo3} data of Posidonia shales are around 0.6 due to incorporation of carbonates into the fraction of strong/brittle minerals (Eqn. 3). For the same reason, pure carbonates (LIM, MAR) are considered brittle by their definition, whereas other classifications yield ductile behavior. For our modified criterion (Eqn. 4), we assume weighting factors for strong and weak components and porosity of 1 and for carbonates of 0.5, reflecting their relative strength at elevated P - T conditions (Fig. 4). Adding porosity in the denominator of Eqn. (4) accounts to some extent for the reduced brittleness of sandstones compared to novaculite.

6. Discussion

Uni- and triaxial tests of black shales at ambient and elevated pressures and temperatures reveal a strong pressure and temperature dependence of the peak stress and hardening/weakening of stress strain curves. Microscopically, semibrittle deformation prevails with fracturing of the stronger minerals and creep of weak phases, which results macroscopically in a gradual transition with increasing pressure and temperature (or simulated depth) from more elastic-brittle deformation with sharp peak stress and sudden stress drop after failure to ductile deformation with smooth post-failure weakening (Figs. 3, 4).

6.1 Comparison of brittleness index values

The brittleness index definitions based on stress-strain behavior generally indicate changing brittleness with changing conditions (Fig. 6). A distinct difference of $B_{preStrain}$ and $B_{resStress}$ values at similar deformation conditions and a decrease of both indices with increasing pressure and temperature, as well as an anisotropy effect due to bedding orientation, was also observed by Holt et al. (2011) on various North sea shales and by Yang et al. (2013) on different North American shales. For given deformation conditions, the absolute magnitudes of B values of a specific rock vary substantially, depending on definition (Fig. 5), but generally reflect correctly the variations of brittleness with rock composition. For example, the brittleness of Barnett and Alum shale is higher than of Posidonia shales, among which Harderode shale shows the highest brittleness. Post failure based definitions in cases show reverse trends, in particular at ambient temperature (Tab. 2), which is probably due to measurement problems. Also, the internal friction based index B_{Mohr} yields higher brittleness of Alum and Barnett shale compared to Posidonia shales at ambient temperature. However,

p [17]

for Posidonia shales B_{Mohr} yields the highest brittleness for Wickensen or Dotternhausen shale (Fig. 7b), which do not correctly reflect the stress-strain behavior. This discrepancy may be related to the few pressure data points available for determination of μ and to the narrow investigated pressure range ($\approx 50 - 100$ MPa), which overlaps with the critical pressure below which the friction coefficient increases non-linearly with pressure (Rybacki et al., 2015). The brittleness definition $B_{tensile}$ based on ambient compressive and tensile strength always results in high values for shales that are in the same range as of the reference rocks (Fig. 7c). As pointed out by Thuro and Spaun (1996), the ratio of σ_C to σ_T , which is a non-normalized version of $B_{tensile}$ (cf., Tab A2), is a very poor indicator for drillability in mining sciences. Instead, the drilling rate correlates much better with the so-called ‘destruction work’, which is the total deformation energy until disintegration (beyond peak stress), determined from cyclic deformation in non-brittle rocks. The destruction work may be also used as a non-normalized brittleness index, somewhat similar to $B_{preWork}$, but requires distinct macroscopic failure of the rock at some point in the post-peak regime, which usually does not occur in the ductile (semibrittle – plastic) deformation regime.

We conclude that (pre-) failure based indices are the most reliable brittleness definitions in line with the observed stress-strain behavior and macroscopic failure characteristics. Comparison of all determined values with the shape of stress-strain curves suggests that $B_{preHarden}$ and $B_{preWork}$ reflects at best the relative change of brittleness with composition and deformation conditions, but also $B_{preStrain}$ may be used as well, which is more simple to determine.

Compared to pre- and post-failure based definitions, the brittleness index based on Young’s modulus is relatively insensitive to a change of deformation conditions, except for the influence of temperature (Figs. 5, 6). Interestingly, at fixed deformation conditions B_{Young} mimics almost the same variation with rock composition as $B_{preWork}$, except for pure p [18]

carbonates (Fig. 7a). B_{Young} may therefore be used as an indicator of relative brittleness in a specific reservoir at given P - T conditions. However, the presence of carbonate beds within shales will be interpreted as relatively brittle, which is not in line with the mechanical behavior.

In general, composition-based indices (B_{comp1} and B_{comp2}) also yield correct estimates of the relative brittleness of different shales at elevated P - T conditions (Fig. 7d), where Barnett shale is the most brittle shale, followed by Alum shale and then Posidonia shales, from which Harderode shale is the most brittle one. However, the definitions B_{comp3} and B_{comp4} suggested by Glorioso and Rattia (2012) and Jin et al. (2014), which incorporate carbonates into the fraction of strong/brittle minerals (Eqn. A1), do not fit to this brittleness sequence, resulting in too high index values for carbonate-rich (Posidonia) shales compared to carbonate-poor (Barnett and Alum) shales (cf., B_{comp3} in Fig. 7d). Compared to B_{comp1} and B_{comp2} incorporation of porosity into the composition-based definition ($B_{porocomp}$) yields more reliable brittleness contrasts of the different investigated rocks, in particular for porous sandstones and shales (Fig. 7d). However, all composition-based indices predict that pure carbonate rocks are either brittle with $B = 1$ (for definitions containing carbonates within the fraction of strong/brittle minerals) or ductile with $B = 0$ (other definitions), which both do not reflect the measured mechanical behavior. For example marble showed almost steady state deformation and homogeneous barreling suggesting $B = 0$, whereas deformation of limestone was semibrittle with a transient stress-strain plateau and localized failure, suggesting $0 < B < 1$ (Fig. 4e). This demonstrates that none of the composition-based indices account for the effect of changing grain size, water content or anisotropic fabric on brittleness. In addition, any change of the mechanical behavior by changing P - T conditions cannot be captured by composition-based indices.

Comparison of our experimental data allows to estimate roughly the absolute magnitude of B values for the onset of predominant ductile behavior. This behavior is characterized by almost steady state deformation and homogeneous barreling of samples without evolution of single shear fractures. In tables 1 and 2 all samples deforming ductile at our applied experimental conditions are indicated by brittleness values given in italic notation. Comparison of these values suggests that predominant ductile deformation predominates for the following brittleness threshold values: $B_{preHarden} < 0.12$, $B_{preWork} < 0.20$, $B_{preStrain} < 0.32$ and $B_{resStress} < 0.19$. The estimated error is about 30% because of the uncertainty associated with the determination of E . These threshold values are in line with most data measured under undrained conditions at a strain rate of $5 \times 10^{-4} \text{ s}^{-1}$, but not with several values measured at lower strain rates (Tab. 2). This indicates that the limits may be lower at drained conditions. For $B_{resStrain}$ no reliable threshold value is available because of the uncertainty in determining the residual strain for ductile deformation. Similarly, no reliable threshold value can be determined for B_{Young} because of its insensitivity to a change of experimental conditions. Using $B_{porocomp}$, the increase of ductility with increasing pressure and temperature may be empirically accounted for by adjusting the weighting factors. For example, if the weighting factor w_{QFP} for strong/brittle minerals in Eqn. (4) is reduced from 1.0 to 0.5, the corresponding brittleness values of shales reduce by about 40% (Tab. 2), which indicates less brittleness. This adjustment can be used for example to account for an increase of pressure from 50 MPa, where the shales showed brittle to semibrittle behavior with pronounced strain weakening after failure, to 100 MPa, for which Posidonia shales showed ductile behavior with minor weakening. The corresponding threshold value is about 0.16.

6.2 Correlations of brittleness with composition and Young's modulus

Representative for deformation-based brittleness indices, the variation of $B_{preWork}$ with porosity and composition at elevated temperatures is shown in Fig. 8. For better readability, we did not include data measured at ambient temperature, where most samples showed brittle behavior (cf., Fig. 4). Although our data set is limited, for Posidonia shales no significant change of $B_{preWork}$ with porosity or the amount of weak phases, carbonates or strong minerals is evident. The same results with respect to composition-dependence were also found for B_{Mohr} and B_{Young} . This agrees with results of Yang et al. (2013), who found no correlation between brittleness indices $B_{preStrain}$ and $B_{resStress}$ and clay content of North American shales, deformed at 20°C and pressures between 10 and 60 MPa.

Expanding the composition range by considering in addition the brittleness of Alum and Barnett samples measured at $P = 50$ MPa and $T = 100^\circ\text{C}$ temperature, $B_{preWork}$ appears to decrease with increasing porosity and carbonate content and to increase with increasing fraction of strong minerals and weak components (Fig. 8). However, these are apparent correlations since the mechanical behavior depends on the relative proportion of all components and not just on a single mineral fraction. For example, low porosity Alum and Barnett shales with few carbonates and a high amount of strong mineral show high brittleness values, but they contain also a high fraction of kerogen and clays (Fig. 1, Tab. 1). Similar apparent correlations with composition were obtained for the peak strength and Young's modulus of the investigated shales (Rybacki et al., 2015). We therefore conclude that ductility does not correlate solely with the clay fraction. Brittle or ductile behavior of shales instead depends also on the fraction of the other components (strong minerals and carbonates), porosity, water content, fabric anisotropy and applied deformation conditions. Nevertheless, $B_{preWork}$ shows a positive correlation with $B_{porocomp}$ at low P - T conditions. However, this progressively weakens with increasing pressure and temperature and shows almost no correlation in the ductile regime without post-failure weakening (below the dotted line in Fig.

8e). Restricting the data to the brittle-semibrittle regime with $B_{preWork} > 0.2$, the brittleness definition $B_{preWork}$ may be determined from the composition-related definition $B_{porocomp}$ by (short-dotted line in Fig. 8e):

$$B_{preWork} = -(0.02 \pm 0.05) + (1.33 \pm 0.20)B_{porocomp}, \quad (13)$$

with a correlation coefficient of $r^2 = 0.84$. To ensure that $B_{preWork} > 0.2$, $B_{porocomp}$ should be > 0.2 as a more conservative estimate. The slope decreases to 1.24 ± 0.05 if the offset is fixed equal zero. It should be mentioned that this relation cannot be applied in deep environments, where deformation is expected to be prominently ductile.

The correlation between $B_{porocomp}$ and the measured (secant) Young's modulus E (cf., Rybacki et al., 2015) is shown in Fig. 9a, revealing a positive correlation at all conditions. Fitting linear relationships for the individual P - T conditions yield almost similar slopes and offsets at given temperature (broken lines in Fig. 9a). Empirical fitting of all data by a power law relationship (dotted line in Fig. 9a) yields the relation:

$$B_{porocomp} = (0.10 \pm 0.01)E^{0.38 \pm 0.04}, \quad (14)$$

with $r^2 = 0.84$. Note, however, that the fit is strongly influenced by the single BAR data point. Eqn. (14) may be used to estimate the composition-based brittleness $B_{porocomp}$ from Young's modulus if only a sonic log and no cuttings are available or vice versa.

Similar to the relation between $B_{preWork}$ and $B_{porocomp}$, the relation between $B_{preWork}$ and E is very poor in the predominantly ductile regime ($B_{preWork} < 0.2$, below the dotted line in Fig. 9b), as expected from the low sensitivity of E at high P - T conditions. Using again all data in the brittle and semibrittle regime with $B_{preWork} > 0.2$, a power-law fit yields a nearly square-root dependence of $B_{preWork}$ on E with (dotted line in Fig. 9b):

$$B_{preWork} = (0.07 \pm 0.01)E^{0.53 \pm 0.07}, \quad (15)$$

with $r^2 = 0.76$. As before, this fit is strongly affected by the single Barnett brittleness value. If a shale is not deforming in the predominantly ductile regime, Eqn. (15) may be used to estimate the short-term brittleness from Young's modulus for E values > 7 GPa (intersection with the $B_{preWork} = 0.2$ line). However, the scatter is relatively large, so that only shales with a static Young's modulus higher than 13 GPa can be treated as non-ductile with some confidence.

For North American shales, Rickman et al. (2008) suggested a brittleness definition based on Young's modulus and Poisson's ratio ν ($B_{elastic}$, c.f., Eqn. A17). In their data compilation, shales with high E show low ν values and vice versa, where the first are stated to be prospective (brittle) and the later to be non-prospective (less brittle or 'ductile'). The authors used for their brittleness calibration a lower limit of $E \approx 7$ GPa for ductile shales and an upper limit of $E \approx 55$ GPa for brittle shales. However, for example Woodford shale shows the inverse relationship between E and ν , i.e., decreasing Young's moduli with decreasing Poisson's ratio (Harris et al., 2011), which indicates that for shales E and ν are not uniquely related. Note that E and ν are linearly connected by the shear modulus G by $E = 2G(1+\nu)$ and to the bulk modulus K by $E = 2K(1-2\nu)$. Therefore, other brittleness indices related to elastic properties were suggested, relying also on K , Lamé parameters or density (cf., Eqns. A18 – A20, Tab. A3).

Based on the measured correlations between static and dynamic Young's moduli of prospective and non-prospective shales from the North American Mid-Continent and South Texas, Britt and Schoeffler (2009) concluded that prospective shales can be characterized solely by static Young's moduli higher than ≈ 24 GPa (3.5 Mpsi). In comparison, our estimate of $E < 7$ -13 GPa for predominantly ductile shales is considerably lower than Britt and Schoeffler's threshold value for prospective shales and coincides with the lower E -limit of

Rickman's calibration. This suggests that shales may be non-prospective even if the short-term deformation behavior is not predominantly ductile, but deform in the semibrittle regime (with E between ≈ 13 and 24 GPa).

It should be mentioned that Rickman et al. (2008) and Britt and Schoeffler (2009) used static Young's moduli for calibration, which may be 20-40% lower than (undrained) dynamic E -moduli (e.g., Yale and Jamieson, 1994; Britt and Schoeffler, 2009; Sone and Zoback, 2013a). In contrast, Young's moduli determined from un- or reloading stress-strain curves fits well to dynamic moduli (Sone and Zoback, 2013a). Unfortunately, for shales the determination of Young's modulus is ambiguous since often no clear linear elastic behavior is evident in the stress-strain curves (Fig. 4). Also, different authors used different conventions to estimate E . As mentioned above, we used the 50%-secant modulus which is about 20-30% higher than the 50%-tangent modulus.

6.3 Relevance for prospectivity of shale reservoirs and hydraulic fracturing stimulation

The amount of gas or oil in place and the prospectivity of shale reservoirs may depend on many, geological, chemical and mechanical factors. The depth and thickness of shale reservoirs, TOC, kerogen type, thermal maturity and porosity, among others, determine the quantity and quality of gas is trapped in pores, fissures and veins or adsorbed at the solid matrix.

For hydrocarbon extraction from low permeability shale reservoirs wells need to be drilled and the formation stimulated by hydraulic fracturing. Stimulation operations aim at increasing the production rate by increasing the degassing rock volume connected to the borehole. Therefore, successful stimulation demands to perform multistage hydrofracs and reactivating

preexisting fractures in the reservoir shale. Usually, proppants are added to the frac fluid to keep the fractures open after fluid pressure release.

Practical experience indicates that the prospectivity of shales correlates with brittleness based on elastic parameters (Grieser and Bray, 2007; Rickman et al., 2008, Britt and Schoeffler, 2009). Unfortunately, the physical meaning and justification of these empirical correlations remains unclear. Rickman et al. (2008) suggest that brittleness determined from Poisson's ratio and Young's modulus (Eq. A17) reflects the ability of a rock to fail under stress and to maintain permeable a fracture, respectively. However, by definition both parameters are related solely to the elastic response and not to inelastic deformation of a rock (e.g., fracturing, healing). Here, we showed that brittleness determined from Young's modulus correlates also with brittleness index values calculated from composition and mechanical deformation at low P-T conditions (Figs. 8, 9). To unravel the significance of brittleness on shale prospectivity, we briefly discuss the relation of brittleness to three main factors that may influence hydrocarbon extraction and reservoir stimulation: 1) the formation and preservation of natural fractures, 2) the initiation and propagation of artificial (hydraulic) fractures, and 3) the healing of induced fractures with time by proppant embedment. All three processes are strongly affected by the mechanical properties of the source rock.

First, the formation of natural fractures within transvers isotropic shales mainly depends on the geological evolution of the reservoir rocks and on tectonic forces and local stress concentrations at inhomogeneities and flaws. Fracture formation is less likely in ductile rocks. Since for shales the peak strength increases with increasing Young's modulus and both parameters correlate with the volumetric fraction minerals and pores (Rybacki et al., 2015), rocks with high brittleness may have abundant fractures compared to more ductile shales with low brittleness. For shales with very low brittleness (i.e., $B_{prework} < 0.2$) the rock will deform inelastically in a more ductile-plastic manner without fracturing, in particular at high

p [25]

pressures and temperatures. Fractures may seal more rapidly by creep and compaction in ductile shales. In addition, shales with a high amount of swell-capable clay minerals like smectite are more prone for self-healing of fractures in the presence of fluids.

Second, easy initiation and propagation of hydraulically induced fractures within the host rock and/or along existing bedding planes, veins or healed fractures will considerably increase the shale prospectivity. Initiation requires preferentially low breakdown pressures that depend on the tensile strength (or Mode I fracture toughness) and on the elastic and inelastic deformation properties, which constrain the magnitude of principal stresses. This can be illustrated by applying the classical elastic Hubert-Willis model for calculating the breakdown pressure P_b of rocks in vertical boreholes (e.g., Jin et al., 2013):

$$(P_b - P_0) = 3(\sigma_h - P_0) - (\sigma_H - P_0) + \sigma_T \quad \text{or} \quad P_b = 3\sigma_h - \sigma_H + \sigma_T - P_0, \quad (16)$$

where σ_h and σ_H are the minimum and maximum horizontal stresses, respectively, σ_T is the tensile strength and P_0 is the pore pressure. At constant pore pressure, the difference $3\sigma_h - \sigma_H$ in Eqn. (16) and therefore P_b is maximum for ductile rocks because their flow strength is low so that the horizontal stresses tends to be nearly equal. In the limiting case of $\sigma_h \approx \sigma_H$ we have $P_b \approx 2\sigma_h + \sigma_T - P_0$. For comparison, assuming $\sigma_H = 2\sigma_h$ for brittle shales yields $P_b \approx \sigma_h + \sigma_T - P_0$, which is by the magnitude of σ_h lower than for ductile rocks.

On the other hand, the permeability of ductile shales may be considerably lower than for brittle shales, which can result in higher (over-hydrostatic) pore pressure. Assuming a maximum pore pressure of $P_0 = \sigma_h$ for ductile shales yields $P_b \approx \sigma_h + \sigma_T$, whereas for permeable brittle shales with a maximum (hydrostatic) pore pressure of $P_0 = P_{hydr}$ we obtain $P_b \approx \sigma_h + \sigma_T - P_{hydr}$. Therefore, for different pore pressures, the breakdown pressure of ductile shales can be up to the magnitude of P_{hydr} higher than of brittle shales, but hydrocarbon extraction is likely more efficient in ductile shales if they are over-pressured.

Following Eqn. (16), P_b increases with increasing tensile strength. The Griffith energy criterion for tensile failure of an elliptical crack under plane strain conditions predicts that $\sigma_T \propto \sqrt{\frac{kE\gamma}{c(1-\nu^2)}}$, where γ is the specific surface area, c is the half crack length and k is a constant (e.g., Paterson and Wong, 2005). Therefore, σ_T (and P_b) are expected to increase with increasing E and ν , which contradicts the brittleness concept based on Young's modulus, for which high E results in high brittleness, i.e., low P_b . Numerical analysis of hydraulic fracturing operations in gas shale also suggests that a high Young's modulus and Poisson's ratio do not favor fracture propagation, which is more sensitive to the type of injection fluids and rates, permeability and tensile strength (Kim and Moridis, 2015).

Linear elastic fracture mechanics uses the fracture toughness K_{Ic} to determine the ability of a brittle rock to resist fracture propagation from a preexisting crack. The Mode I fracture toughness K_{Ic} was found to be linearly related to the tensile strength, e.g., Jin et al., 2014; Wang et al., 2007. Therefore, high K_{Ic} suggest high breakdown pressure or poor 'fracability'. Accordingly, the fracture toughness was more recently incorporated into the brittleness concept, indicating low fracability of shales with high fracture toughness values (Jin et al., 2014, 2015; Guo et al., 2015, cf. Eqns. A34-A36, Tab. A5). This is in line with indentation hardness-based brittleness concepts, which predict decreasing brittleness with increasing K_{Ic} (cf., Eqns. A27, A28, Tab. A4). However, at larger depth the magnitude of σ_T is small compared to the in-situ stresses, so that the influence of tensile strength or fracture toughness on prospectivity may be ignored. In addition, measurements of fracture toughness at elevated pressure and temperature are almost missing so far.

It should be noted that Eqn. (16) neglects poroelastic effects and the fluid pressure distribution within pre-existing fractures. Fracture mechanics approaches indicate that P_b increases with increasing angle between the orientation of the maximum principal stress and the fracture

orientation and for a non-linear pressure distribution inside fractures (Jin et al., 2013, Stöckhert et al., 2015). If the propagating hydraulic fracture intersects natural fractures, these may be reactivated, depending on their orientations. Fracture reactivation may be influenced by adjusting the injection rate (or fluid viscosity) as demonstrated by laboratory hydraulic fracturing experiments on shales (Cheng et al., 2015).

Using a poro-elastic deformation approach and assuming constant strain (rate) boundary conditions, Herwanger et al. (2015) suggested that for a layered two-phase medium with different (elastic) brittleness of each layer the magnitude of the minimum horizontal stresses within the layers vary with total strain. In their example of a (highly brittle) sandstone layer situated at about 2.5 km depth in between (less brittle) mudstone, the minimum horizontal stress at low strain conditions ($\approx 0.03\%$) is slightly lower (≈ 1 MPa) in sandstone than in the mudstone and by about the same magnitude higher at slightly higher tectonic strain (0.04%). For the low strain case, a hydraulic fracture generated in the sandstone will further propagate within this layer due to the lower minimum horizontal stress compared to the adjacent mudstone, which supports the expectation that rocks with high (elastic) brittleness represent preferred formations for hydraulic fracturing stimulation. In contrast, at higher strain the situation is reversed and the fracture propagates into the mudstone with low brittleness. Therefore, the authors concluded that the brittleness index is not a good (unique) indicator for the prospectivity of shales with respect to hydraulic fracturing. However, shales do not deform in a purely poro-elastic manner, but tends to creep inelastically even at very low stress and strain magnitudes (Sone and Zoback, 2013b) allowing to relax differential stresses (Sone and Zoback, 2014). In addition, the constant strain (-rate) assumption used by Herwanger et al. (2015) yields an upper stress (Voigt) bound in the considered two-phase system, but the mechanical behavior of shales seems to be more close to the lower constant stress (Reuss) bound (Rybacki et al., 2015).

The third aspect that affects the prospectivity of shale plays over time is healing of (propped) fractures, which strongly reduces the gas inflow. Rocks with low brittleness are expected to have a low self-propping potential and exhibit easy mechanical indentation of added proppants by the acting tectonic stresses. However, the associated healing behavior is constrained by the long-term creep behavior of shales, which may be different from the short-term brittleness. Small strain deformation tests ($< 0.1\%$) on North American shales at normal temperature and pressure up to 60 MPa indicated that the creep strain after 3 h increased linearly with applied differential stress and that the corresponding slopes correlated inversely with the measured Young's moduli (Sone and Zoback, 2013b). This suggests that the creep behavior may be estimated from the Young's modulus, at least under the tested conditions, and that shales with high (elastic) brittleness will exhibit less fracture healing. It should be noted that the creep measurements performed by Sone and Zoback (2013b) indicate Newton viscous deformation behavior of shales independent of the applied confining pressure. However, for longer creep durations at higher stress/strain and elevated temperature the creep rate and strength are expected to be non-linearly correlated, depending on the activated creep mechanisms (e.g., dislocation glide and creep, diffusive mass transfer, dissolution precipitation processes). So far, relevant creep data are scarce. Long-term creep experiments at elevated pressure and temperature are required to constrain the fracture healing behavior and to verify if the healing behavior can be assessed from conventional brittleness indices.

7. Conclusions

Experimental deformation of black shales with different composition and porosity at ambient and elevated pressures and temperatures reveals a transition from brittle to semibrittle deformation behavior at high confining pressure and temperature. In comparison, a variation

of strain rate over several orders of magnitude has a small effect on the deformation behavior, whereas it is significantly affected by a change of water content or bedding orientation.

For given rock bulk composition and deformation conditions, the magnitude of brittleness B strongly depends on the used index definition. Pre-failure stress and strain-based indices should be preferred for determination of brittleness, whereas B values determined from ambient compressive and tensile strength gave no reliable results. In particular, indices defined by energy consumption and hardening behavior best represent changes in mechanical behavior.

B values vary substantially with applied pressure and to lesser extent also with temperature, loading rate and water content.. Composition-based brittleness indices generally show similar trends as those derived from stress-strain behavior, in particular if porosity is included, but do not account for varying deformation conditions. Brittleness cannot be estimated from the fraction of individual phases, e.g. clays, alone, but depend on the proportion of all components. Indices treating carbonates as a strong phase predict too high brittleness for carbonate-rich rocks.

For pre-failure based definitions, we estimated upper threshold values for predominantly ductile deformation at undrained conditions (e.g., $B_{preWork} < 0.2$). However, at low pressures and temperatures, roughly corresponding to $\lesssim 4$ km depth, , where deformation is mainly brittle or semibrittle, brittleness calculated from stress-strain behavior correlates with brittleness determined from composition (Eqn. 13) and from the static Young's modulus (Eqn. 15). This allows estimates of brittleness in shallow environments from core (for $B_{porocomp} \gtrsim 0.15$ -0.20) and sonic logs (for $E \gtrsim 7$ -13 GPa, or $B_{Young} \gtrsim 0.08$ -0.16), respectively.

Using the concept of brittleness in shallow environments can help to judge upon the prospectivity of shale reservoirs. Rocks with higher brittleness may form and preserve natural

fractures (if not too strong), facilitate hydraulic fracturing simulations by low breakdown pressures due to high anisotropy of the in-situ stress field and probably low fracture healing rates. On the other hand, pores within high brittleness shales may be less over-pressured, hydraulic fractures may propagate in more ductile shales, and at low depth, where the influence of tensile strength on the breakdown pressure cannot be ignored, brittle rocks with typically high Young's modulus and fracture toughness may have a higher breakdown pressure than ductile rocks, suggesting poor fracability.

Appendix A: Brittleness Index Definitions

Depending on discipline, e.g., hard rock mechanics, soil mechanics, petroleum science or mining science, a variety of brittleness index definitions was suggested in the past years (e.g., Hucka and Das, 1974; Andreev, 1995; Holt et al., 2011; Yarali and Kahraman, 2011; Yang et al., 2013; Meng et al., 2015 and references therein). In the following, we briefly summarize the suggested definitions without claiming completeness. These are categorized here into brittleness index terms based on a) composition, b) stress-strain properties in the pre- and post-failure regime, c) elastic parameters, d) indentation behavior, and e) miscellaneous definitions.

A.1 Composition-based indices

Mineralogy-based approaches (Eqns. A1-A2) regard solely the rock composition, which can be determined from cuttings and cores. Quartz and some other minerals are considered to be very strong and brittle, whereas clays and organic components are treated as weak and ductile. The corresponding definitions are given in Tab. A1. The definitions are normalized, yielding a brittleness of $B = 1$ for brittle and $B = 0$ for ductile rocks.

A.2 Indices based on deformation behavior

A large number of brittleness index definitions were proposed that are based on the mechanical deformation behavior of rocks in (tri-) axial deformation experiments in terms of stress, strain, energy, or hardening/weakening ratios (Tab. A2). Their determination requires intact rock cores, which should be preserved without major alteration in terms of humidity and unloading cracks. One of the earliest definitions was suggested by Heard (1960), who, based on deformation experiments on limestone, arbitrarily defined brittle behavior as the point at which less than 3% strain can be induced without loss in cohesion and ductile behavior if a rock can be deformed for more than 5% strain, with a transitional (semibrittle) regime in between.

Here, the various proposed indices are subdivided into those related to a) (pre-) failure behavior (Eqns. A3-A10) and those related to b) post failure behavior (Eqns. A11-A16). Many definitions rely on the stress or strain at final rock failure, which can be easily determined in the brittle regime. In the semibrittle and plastic regime, where often no clear failure point can be determined, the peak stress-strain conditions may be used instead. Some of these definitions can be formulated in two different ways, non-normalized or normalized to a range of 0 - 1. For post failure-based definitions, the residual strength, strain and post-failure weakening behavior was used to quantify brittleness, which requires a stiff deformation apparatus for accurate measurements. In particular, advanced controlling techniques are required (e.g., via acoustic emission rate in fast-reacting servo-controlled machines) to be able to measure the so-called intrinsic brittleness of 'superbrittle' Class II rocks, which show a positive weakening modulus after failure. Using standard deformation apparatuses, the stored energy in the loading system usually yields Class I deformation (negative weakening slope M ,

cf., Fig. 2). With two exceptions (Eqns. A9-A10), the brittleness indices based on deformation behavior can be determined at any pressure-temperature conditions.

A.3 Indices based on elastic parameters

Relying on the experience of prospective shales, brittleness indices determined from elastic parameters were proposed in petroleum science (Eqns. A17-A21, Tab. 3). They can be estimated from conventional borehole logging. Most often quoted is the brittleness definition related to Young's modulus and Poisson's ratio (Eqn. A17), which are believed to describe the ability of a rock to maintain a fracture once its fractures and the ability to fail under stress, respectively (Rickman et al., 2008). Britt and Schoeffler (2009) instead suggested that the characteristics of prospective shales are given by a static Young's modulus higher than 3.5 Mpsi (≈ 24 GPa).

A.4 Indices based on indentation testing

Several definitions based on indentation tests at ambient conditions were proposed in mining, drilling, and ceramic science (Eqns. A22-A28, Tab. 4). Unfortunately, most of them are not calibrated, at least for rocks.

A.5 Other definitions

Several other brittleness index definitions were proposed, based on core diskings, energy consumption during rock crushing, the overconsolidation ratio of mudrocks, and combined formulations (Eqns. A29-A36, Tab. 5). In soil mechanics, the overconsolidation ratio $OCR =$

$\sigma_{maxH}/\sigma_{act}$ is defined as the ratio of the maximum effective stress σ_{maxH} that a rock was subjected to in history to the current effective stress σ_{act} . Considering tectonic regimes of normal faulting, OCR is a proxy of tectonic uplift. Overconsolidated (OC) rocks are those with $OCR > 1$ and for normally consolidated (NC) rocks $OCR = 1$.

Most recently, combinations of different brittleness indices or the combination of normalized brittleness with fracture toughness values were proposed as index definitions, trying to account for the hydraulic fracturing process during shale reservoir stimulation. The latter are explicitly termed ‘fracability’. Other more advanced definitions based on linear elastic fracture mechanics are given by Bazant and Kazemi (1990) and Carpinteri (1991), which are quite complex and not listed here.

Acknowledgements

We like to thank the GASH and GeoEn sponsors and teams for financial support and discussions, Stefan Gehrman for sample and thin section preparation, and Michael Naumann for assistance with deformation experiments in the Paterson apparatus. Two anonymous reviewers provided numerous useful comments that helped improving the manuscript.

References

- Altindag, R. (2002) The evaluation of rock brittleness concept on rotary blast hole drills. J. S. Afr. Inst. Min. Metall. 102, 61-66.
- Andreev, G.E. (1995) Brittle failure of rock materials. Balkema, Rotterdam, 446pp.

- Berard, T., Liu, Q., Dubost, F.X., Jing, B. (2012) A screening process for shale gas prospecting. SPE paper 154736, 19pp.
- Bazant, Z.P., Kazemi, M.T. (1990) Determination of fracture energy, process zone length and brittleness number from size effect, with application to rock and concrete. *Int. J. Fracture* 44, 111-131.
- Bieniawski, Z.T., Hawkes, I. (1978) Suggested methods for determining tensile strength of rock materials. *Int. J. Rock Mech. Min. Sci. Geomech. Abstr.* 15, 99-103.
- Britt, L.K., Schoeffler, J. (2009) The geomechanics of a shale play: What makes a shale prospective! SPE paper 125525, 9pp.
- Carpinteri, A. (1991) Size-scale transition from ductile to brittle failure: structural response vs. crack growth resistance curve. *Int. J. Fract.* 51, 175-186.
- Chen, J.J., Zhang, G.Z., Chen, H.Z., Yin, X.Y. (2014) The construction of Shale rock physics effective model and prediction of rock brittleness. SEG Denver Annual Meeting SEG-2014-0716, 2861-2865.
- Cheng, W., Jin, Y., Chen, M. (2015) Reactivation mechanism of natural fractures by hydraulic fracturing in naturally fractured shale reservoirs. *J. Nat. Gas Sci Eng.* 23, 431-439.
- Copur, H., Bilgin, N., Tuncdemir, H., Balci, C. (2003) A set of indices based on indentation tests for assessment of rock cutting performance and rock properties. *J. S Afr. Inst. Min. Metall.* 103, 589-599.
- Denkhaus, H.G. (2003a) Brittleness and drillability. *J. S. Afr. Inst. Min. Metall.* 103, 523-524.
- Denkhaus, H.G. (2003b) Second reply to R. Altindag 'Brittleness and drillability'. *J. S. Afr. Inst. Min. Metall.* 103, 527.
- Evans, B., Fredrich, J.T., Wong, T.F. (1990) The brittle-ductile

transition in rocks: recent experimental and theoretical progress. In: Duba, A.G., Durham, W.B., Handin, J.W., Wang, H.F. (Eds.) The brittle-ductile transition in rocks. The Heard volume, AGU Geophys. Monogr. 56, Washington, 1-20.

Evans, B., Kohlstedt, D.L. (1995) Rheology of Rocks. In: Ahrens, T.J. (Ed.) Rock Physics and Phase Relations: A Handbook of Physical Constants, Ref. Shelf. AGU, Washington, 148-165.

Fjaer, E., Holt, R.M., Horsrud, P., Raaen, A.M., Risnes, R. (2008) Petroleum related rock mechanics (2nd ed.). Elsevier, Amsterdam, 491pp.

Glorioso, J.C., Rattia, A. (2012) Unconventional reservoirs: Basic petrophysical concepts for shale gas. SPE paper 153004, 36pp.

Grieser, B., Bray, J. (2007) Identification of production potential in unconventional reservoirs. SPE paper 106623, 6pp.

Guo, Z., Li, X., Chapman, M. (2012) Exploring the effect of fractures and microstructure on brittleness index in the Barnett shale. Conference paper SEG-2012-0771, 4pp.

Guo, J.C., Luo, B., Zhu, H.Y., Wang, Y.H., Zhao, X. (2015) Evaluation of fracability and screening of perforation interval for tight sandstone gas reservoir in western Sichuan Basin. J. Nat. Gas Sci. Eng. 25, 77-87.

Hajiabdolmajid, V., Kaiser, P. (2003) Brittleness of rock and stability assessment in hard rock tunneling. Tunnelling Underground Space Technol. 18, 35-48.

Harris, N.B., Miskimins, J.L., Mnich, C.A. (2011) Mechanical anisotropy in the Woodford Shale, Permian Basin: Origin, magnitude, and scale. Leading Edge 30, 3, 284-291.

Heard, H.C. (1960) Transition from brittle fracture to ductile flow in Solnhofen limestone as a function of temperature, confining pressure, and interstitial fluid pressure. *Geol. Soc. Am. Mem.* 79, 193-226.

Herwanger, J.V., Bottrill, A.D., Mildren, S.D. (2015) Uses and abuses of the brittleness index with applications to hydraulic stimulation. *SPE paper* 178678, 9pp.

Holt, R.M., Fjaer, E., Nes, O.M., Alassi, H.T. (2011) A shaly look at brittleness. *ARMA paper* 11-366, 10pp.

Holt, R.M., Fjaer, E., Stenebraten, J.F., Nes, O.M. (2015) Brittleness of shales: relevance to borehole collapse and hydraulic fracturing. *J. Petrol. Sci. Eng.* 131, 200-209.

Huang, X.R., Huang, J.P., Li, Z.C., Yang, Q.Y., Sun, Q.X., Cui, W. (2015) Brittleness index and seismic rock physics model for anisotropic tight-oil sandstone reservoirs. *Appl. Geophys.* 12, 11-22.

Hucka V., Das, B. (1974) Brittleness determination of rocks by different methods. *Int. J. Rock Mech. Min. Sci. & Geomech. Abstr.* 11, 389-392.

Ingram, G.M., Urai, J.L. (1999) Top-seal leakage through faults and fractures: the role of mudrock properties. In: Alin, A.C., Fleet, A.J., Macquaker, J.H.S. (Eds.), *Muds and Mudstones: Physical and Fluid Flow Properties*. *Geol. Soc. London Spec. Publ.* 158, 125-135.

Jaeger, J.C., Cook, N.G.W., Zimmerman, R.W. (2007) *Fundamentals of rock mechanics* (4th ed.). Blackwell, Oxford, 468pp.

Jarvie, D.M., Hill, R.J., Ruble, T.E., Pollastro, R.M. (2007) Unconventional shale-gas systems: the Mississippian Barnett shale of north-central Texas as one model for thermogenic shale-gas assessment. *AAPG Bulletin* 91, 475-499.

Jin, X., Shah, S.N., Roegiers, J.C. (2013) Breakdown pressure determination – a fracture mechanics approach. *SPE paper* 16634, 16pp.

Jin, X., Shah, S.N., Roegiers, J.C., Zhang, B. (2014) Fracability evaluation in shale reservoirs – an integrated petrophysics and geomechanics approach. SPE paper 168589, 14pp.

Jin, X., Shah, S.N., Roegiers, J.C., Zhang, B. (2015) An integrated petrophysics and geomechanics approach for fracability evaluation in shale reservoirs. SPE paper 168589, 9pp.

Kahraman, S., Altindag, R. (2004) A brittleness index to estimate fracture toughness. *Int. J. Rock Mech. Min. Sci.* 41, 343-348.

Kim, J., Moridis, G.J. (2015) Numerical analysis of fracture propagation during hydraulic fracturing operations in shale gas systems. *Int. J. Rock Mech. Min. Sci.* 76, 127-137.

Lawn, B.R., Jensen, T., Arora, A. (1976) Brittleness as an indentation size effect. *J. Mater. Sci. Lett.* 11, 573-575.

Lawn, B.R., Marshall, D.B. (1979) Hardness, toughness, and brittleness; an indentation analysis. *J. Am. Cer. Soc.* 62, 347-350.

Meng, F., Zhou, H., Zhang, C., Xu, R., Lu, J. (2015) Evaluation methodology of brittleness of rock based on post-peak stress-strain curves. *Rock Mech Rock Eng.* 48, 1787-1805.

Mullen, M., Roundtree, R., Barree, B. (2007) A composite determination of mechanical rock properties for stimulation design (What to do when you don't have a sonic log). SPE paper 108139, 13pp.

Mullen, M., Enderlin, M. (2012) Fracability index – More than just calculating rock properties. SPE paper 159755, 10pp.

Nygaard, R., Gutierrez, M., Bratli, R.K., Hoeg, K. (2006) Brittle-ductile transition, shear failure and leakage in shales and mudrocks. *Marine Petrol. Geol.* 23, 201-212.

- Quinn, J.B., Quinn, G.D. (1997) Indentation brittleness of ceramics: a fresh approach. *J. Mater. Sci.* 32, 4331-4346.
- Paterson, M.S. (1970) A high-pressure, high temperature apparatus for deformation. *Int. J. Rock Mech. Min. Sci.* 7, 517-526.
- Paterson, M.S., Wong, T.F. (2005) *Experimental rock deformation – The brittle field.* Springer Berlin, 347pp.
- Rickman, R., Mullen, M., Grieser, B., Kundert, D. (2008) A practical use of shale petrophysics for stimulation design optimization: All shale plays are not clones of the Barnett shale. *SPE paper 115258*, 11pp.
- Rutter, E. (1986) On the nomenclature of mode of failure transitions in rocks. *Tectonophysics* 122, 381-387.
- Rybacki, E., Reinicke, A., Meier, T., Makasi, M., Dresen, G. (2015) What controls the mechanical properties of shale rocks? – Part I: Strength and Young's modulus. *J. Petrol. Sci.* 135, 702-722.
- Sehgal, J., Nakao, Y., Takahashi, H., Ito, S. (1995) Brittleness of glasses by indentation. *J. Mat. Sci. Lett.* 14, 167-169.
- Sharma, R.K., Chopra, S. (2012) New attribute for determination of lithology and brittleness. *SEG Annual Meeting Las Vegas, SEG 2012-1389*, 1065-1069.
- Smolczyk, U, Gartung, E. (1979) Geotechnical properties of a soft Keuper sandstone, *Proc. 4th ISRM Congr. Montreux*, 639-644.
- Sone, H., Zoback, M.D. (2013a) Mechanical properties of shale-gas reservoir rocks – Part 1: Static and dynamic elastic properties and anisotropy. *Geophys.* 78, D381-D392.

Sone, H., Zoback, M.D. (2013b) Mechanical properties of shale-gas reservoir rocks – Part 2: Ductile creep, brittle strength, and their relation to the elastic modulus. *Geophys.* 78, D393-D402.

Sone, H., Zoback, M.D. (2014) Time-dependent deformation of shale gas reservoir rocks and its long-term effect on the in situ stress state. *Int. J. Rock Mech. Min. Sci.* 69, 120-132.

Stöckhert, F., Molenda, M., Brenne, S., Alber, M. (2015). Fracture propagation in sandstone and slate - Laboratory experiments, acoustic emissions and fracture mechanics. *J. Rock Mech. Geotech. Eng.* 7, 237-249.

Tarasov, B., Potvin, Y. (2013) Universal criteria for rock brittleness estimation under triaxial compression. *Int. J. Rock Mech. Min. Sci.* 59, 57-69.

Thuro, K., Spaun, G. (1996) Introducing the ‘destruction work’ as a new rock property of toughness referring to drillability in conventional drill- and blast tunneling. In: Barla, G. (Eds), Eurock’96. Prediction and performance in rock mechanics and rock engineering 2. Balkema, Rotterdam, 707-713.

Tiryaki, B. (2006) Evaluation of the indirect measures of rock brittleness and fracture toughness in rock cutting. *J. S. Afr. Inst. Min. Metall.* 106, 407-424.

Wang, J.J., Zhu, J.G., Chiu, C.F., Zhang, H. (2007) Experimental study on fracture toughness and tensile strength of a clay. *Eng. Geol.* 94, 65-74.

Wang, F.P, Gale, J.F.W. (2009) Screening criteria for shale-gas systems. *Gulf Coast Ass. Geol. Soc. Trans.* 59, 779-793.

Yagiz, S. (2009) Assessment of brittleness using rock strength and density with punch penetration test. *Tunnell. Undergr. Space Technol.* 24, 66-74.

Yale, D.P., Jamieson, W.H. (1994) Static and dynamic rock mechanical properties in the Hugoton and Panoma Fileds, Kansas. SPE paper SPE 27939, 209-219.

Yang, Y., Sone, H., Hous, A., Zoback, M.D. (2013) Comparison of brittleness indices in organic-rich shale formations. ARMA paper 13-403, 7 pp.

Yarali, O., Kahraman, S. (2011) The drillability assessment of rocks using different brittleness values. Tunnell. Undergr. Space Technol. 26, 406-414.

Figure Captions

Figure 1: Ternary diagram of shale composition (in vol%). Mechanically strong phases are quartz (Qtz), feldspar (Fsp) and pyrite (Py), Cb is carbonate (intermediate strong), and weak components are clay (Cly) and kerogen (TOC). Φ is porosity.

Figure 2: Typical stress-strain curve of a viscoelastic rock (grey curve), approximated by linear elastic deformation with subsequent hardening until failure and post-failure stress decrease to the residual frictional strength (black solid lines). E is Young's modulus, H is hardening, M is descendant modulus. ϵ_{ini} , ϵ_{el} , ϵ_{inel} , ϵ_{max} , ϵ_{fail} , ϵ_{res} are the strain for onset of dilatancy, elastic strain, inelastic strain, strain at peak stress, failure strain, and residual strain, respectively. σ_{el} , σ_{max} , σ_{fail} , σ_{res} are the corresponding differential stress values. Note that the failure strain may be larger than the strain at peak stress and that for semibrittle materials the residual stress and strain may be estimated from the intersection of M and the linearized slope of the final sliding section of the stress-strain curve.

Figure 3: Stress-strain curves of black shales deformed at different pressures (a), temperatures (b), strain rates (c), and water content and orientation (d). Deformation conditions and composition are indicated. DOT is Dotternhausen Posidonia shale, WIC is Wickensen

Posidonia shale and ALM is Alum shale. T and || indicate loading normal and parallel to bedding, respectively.

Figure 4: Stress-strain curves of shales deformed at uniaxial conditions of $T = 20^{\circ}\text{C}$ and $P = 0.1\text{ MPa}$ (a) and triaxial conditions of $P = 50, 100\text{ MPa}$ and $T = 20^{\circ}$ (b), 100°C (c) and 200°C (d). HAR is Harderode (Posidonia) shale, HAD is Hadessen (Posidonia) shale and BAR is Barnett shale. The stress-strain curves of reference samples composed of the main constituents of shale and deformed at $P = 50, T = 100^{\circ}\text{C}$ are shown in (e). GRA is granite, NOV is novaculite, GAB is gabbro, FST and BST are sandstones, LIM is limestone, MAR is marble, and COA is black coal. Deformation conditions and composition are indicated. T and || indicate loading normal and parallel to bedding, respectively. Note different scales.

Figure 5: Comparison of brittleness indices based on pre- (Eqns. 8-10) and post-failure deformation behavior (Eqns. 11-12) and Young's modulus (Eqn. 5), determined for WIC (a) and HAR (b) shales. Deformation conditions are indicated. B and D denote brittle and ductile behavior, respectively.

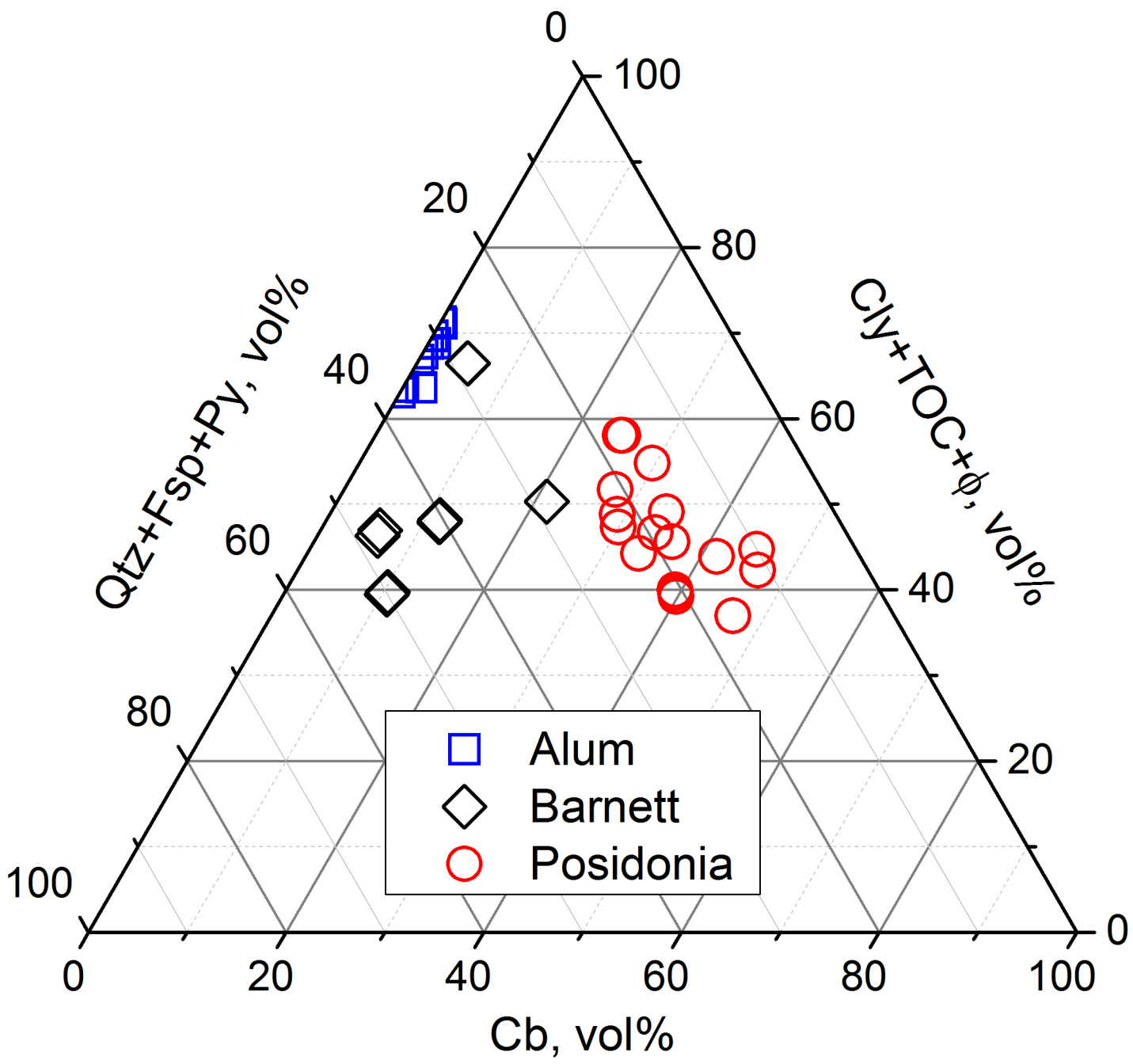
Figure 6: Influence of pressure (a), temperature (b), strain rate (c) and water content (d) on brittleness of shales using selected definitions based on pre- and post-failure behavior and Young's modulus. Deformation conditions are indicated. DOT and WIC samples are deformed normal to bedding and ALM samples parallel to bedding.

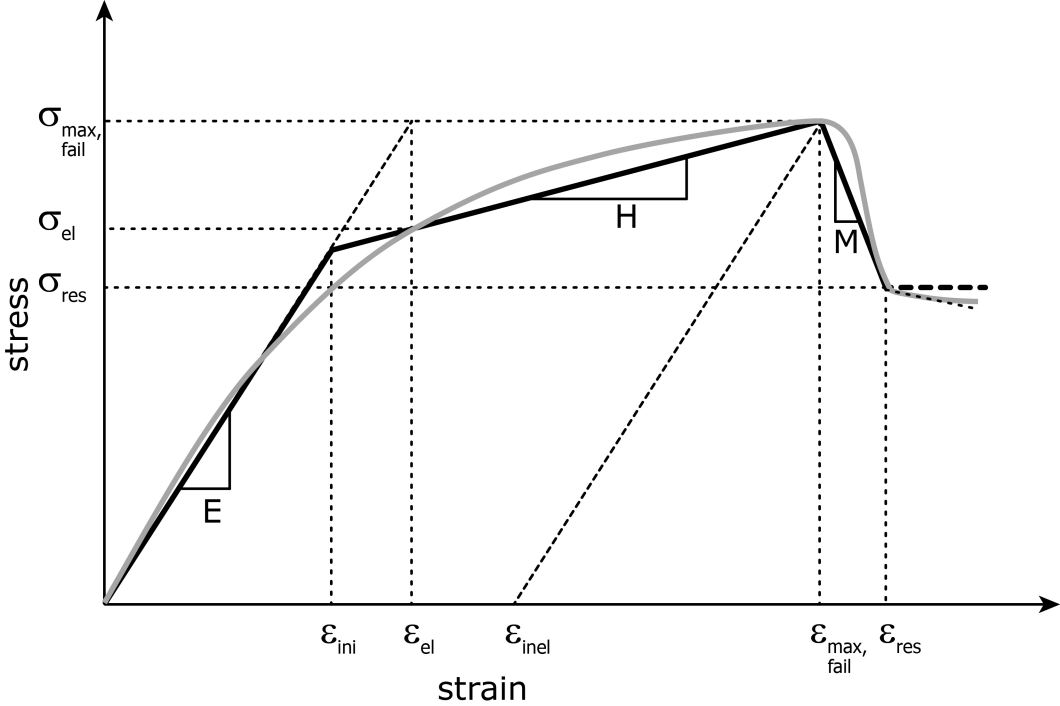
Figure 7: Brittleness index values of shales and reference samples calculated (a) from mechanical behavior and Young's modulus (Eqns. 9, 11, 5), (b) coefficient of internal friction (Eqn. 7), (c) tensile and uniaxial compressive strength (Eqn. 6), and (d) composition (Eqns. 1-4). T and || indicate loading normal and parallel to bedding, respectively. Deformation conditions are indicated. ALM = Alum shale, BAR = Barnett shale, Posidonia shales = DOT = Dotternhausen, WIC = Wickensen, HAR = Harderode, and HAD = Haddessen = HAD,

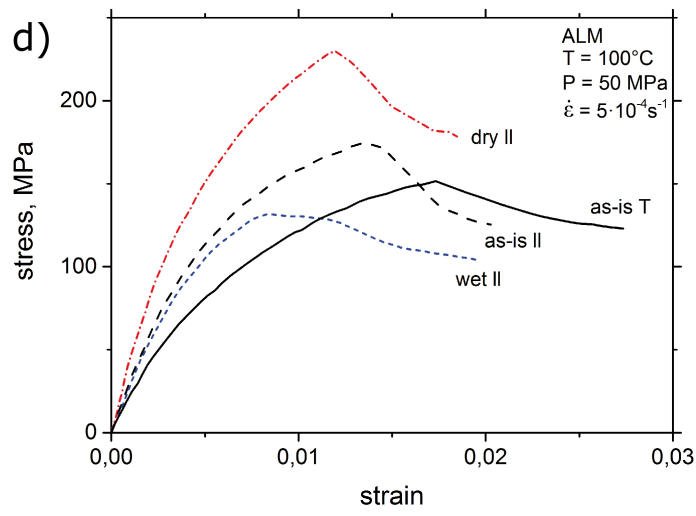
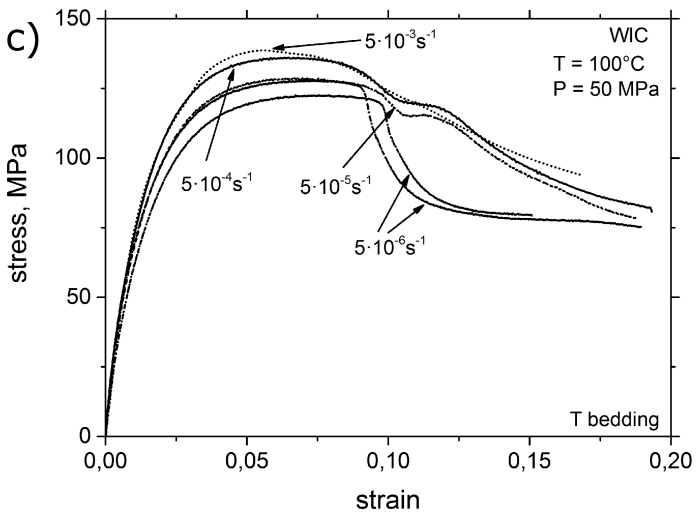
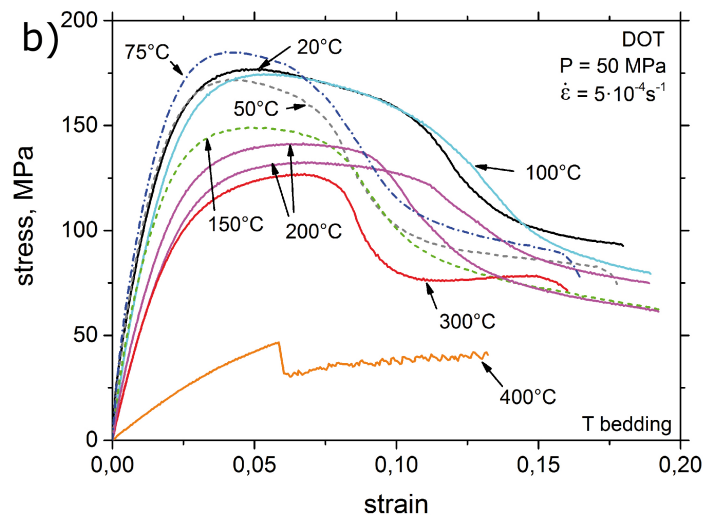
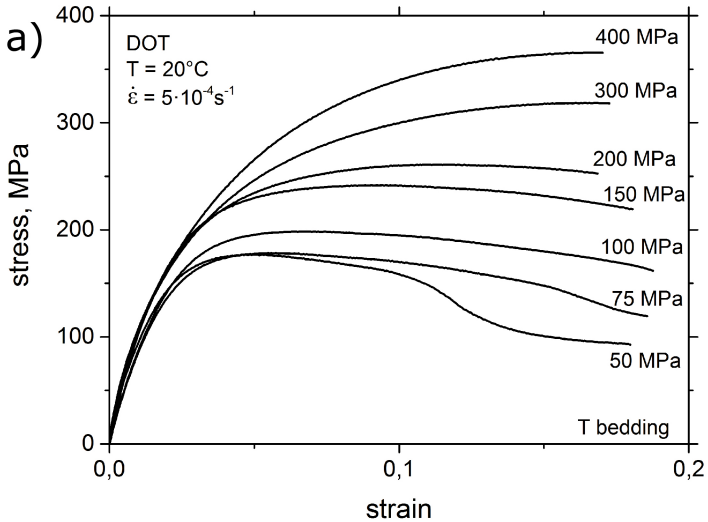
NOV = Arkansas novaculite, GAB = Westerly granite, FST = Flechtingen sandstone, BST = Bentheim sandstone, LIM = Solnhofen limestone, MAR = Carrara marble, COA = black coal.

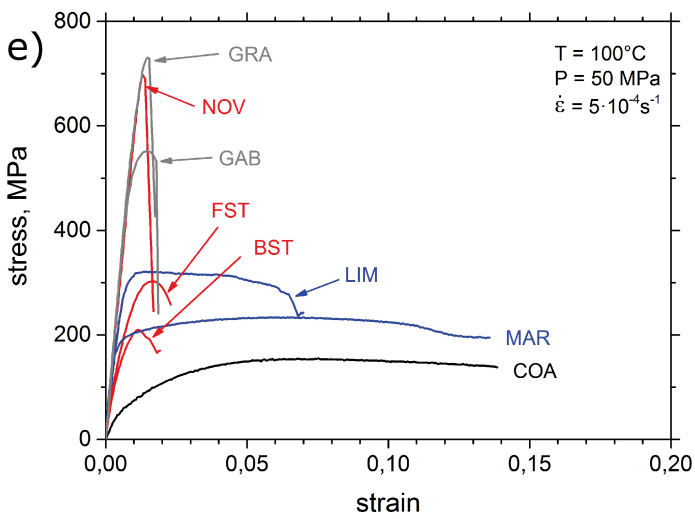
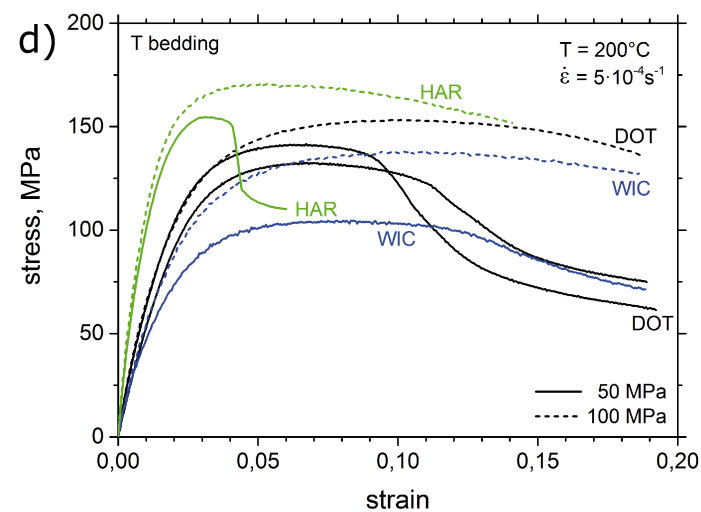
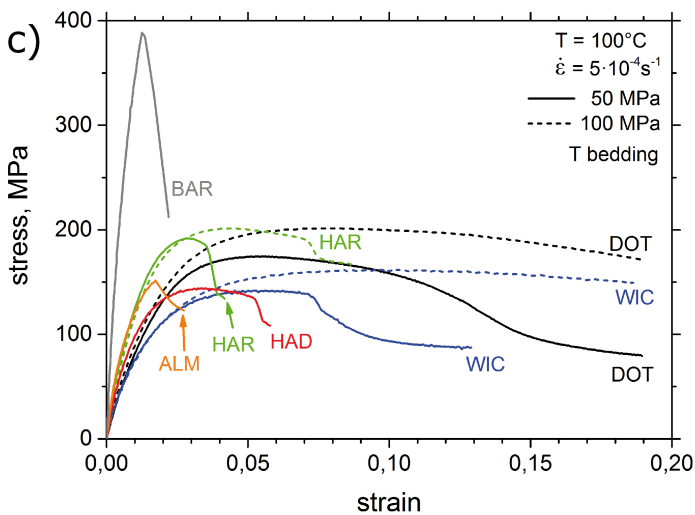
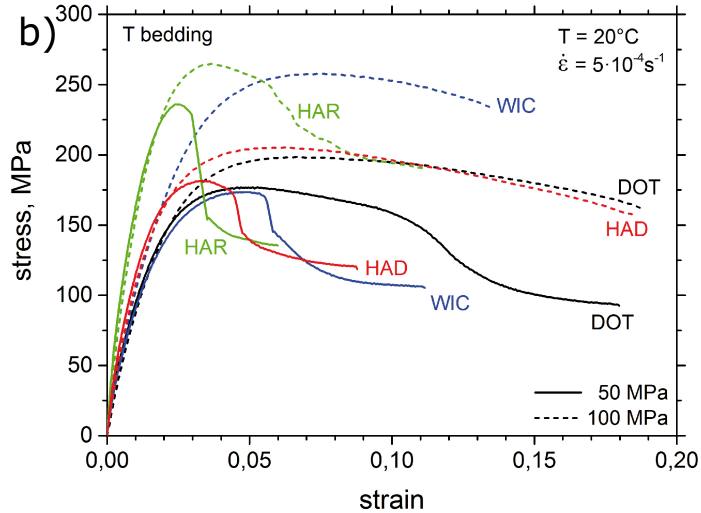
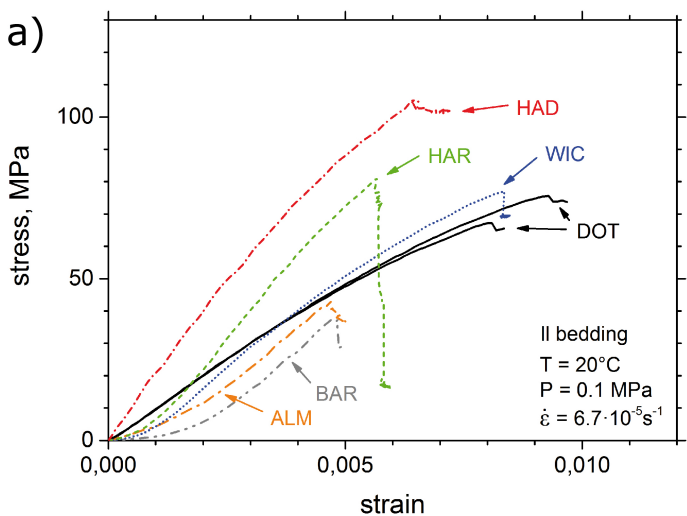
Figure 8: Brittleness index $B_{preWork}$ of Posidonia shales (unlabeled symbols) and Alum (ALM) and Barnett (BAR) shales versus porosity (a), fraction of weak components (b), carbonates (c), strong minerals (d), and $B_{porocomp}$ (e). Deformation conditions are indicated. Broken lines in (e) show linear fits for individual P - T conditions (see inset). Dotted line is a linear fit (Eqn. 13) to all data of samples showing pronounced post-failure weakening, i.e., above the horizontal dotted line of $B_{preWork} = 0.2$.

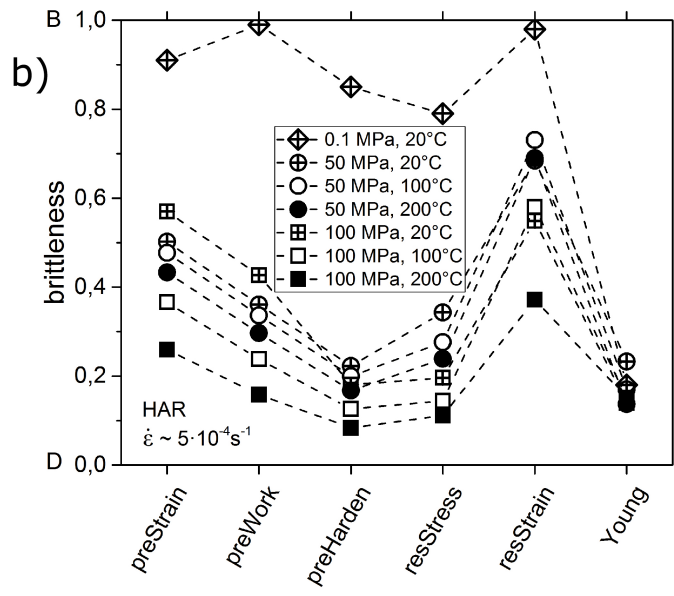
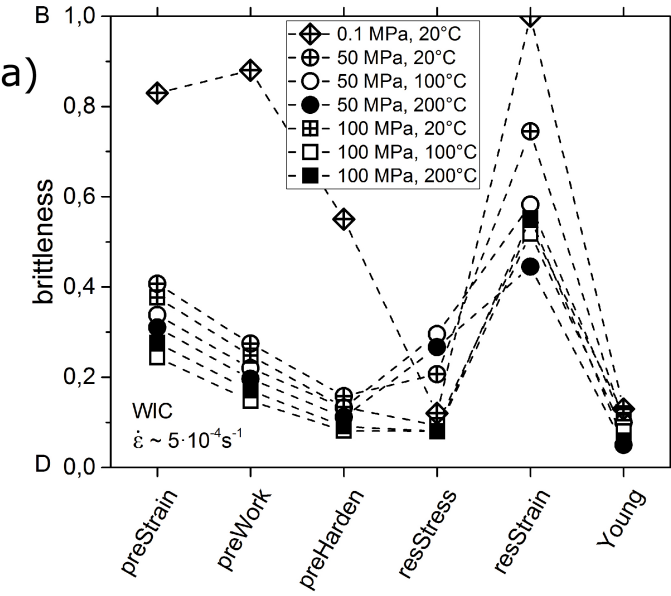
Figure 9: Brittleness indices $B_{porocomp}$ (a) and $B_{preWork}$ (b) versus Young's modulus E . Unlabeled symbols represent Posidonia shales, ALM is Alum shale, BAR is Barnett shale. Linear fits (broken lines) for given P - T conditions at given in insets. Dotted lines show empirical power-law fits for all data (a, cf., Eqn. 14) and for $B_{preWork} > 0.2$ (b, cf., Eqn. 15).

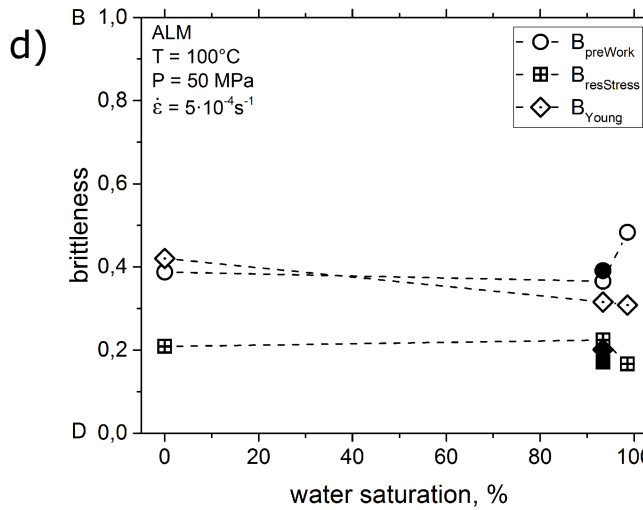
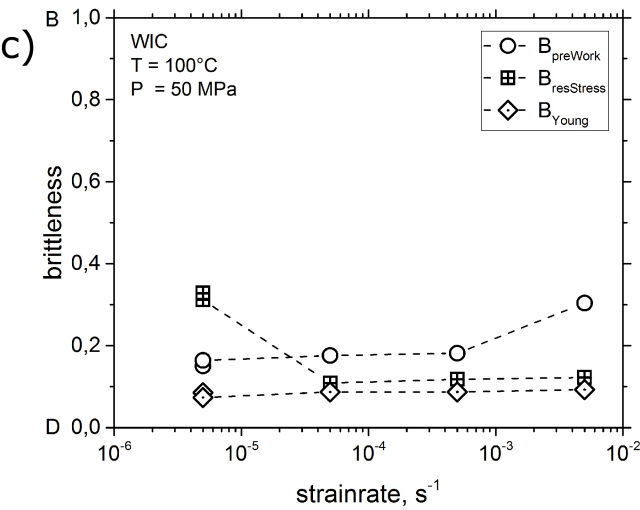
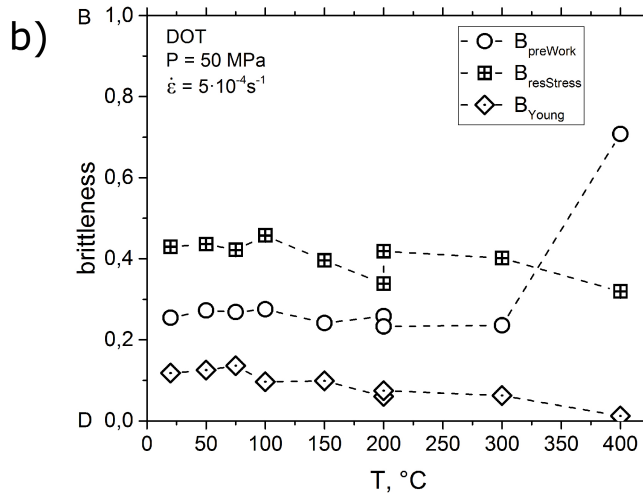
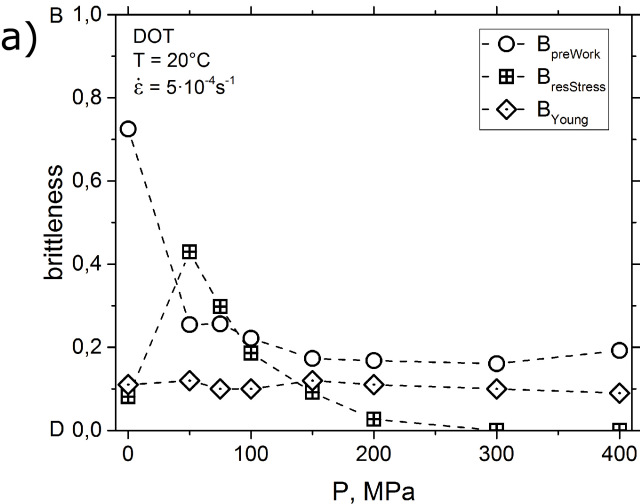


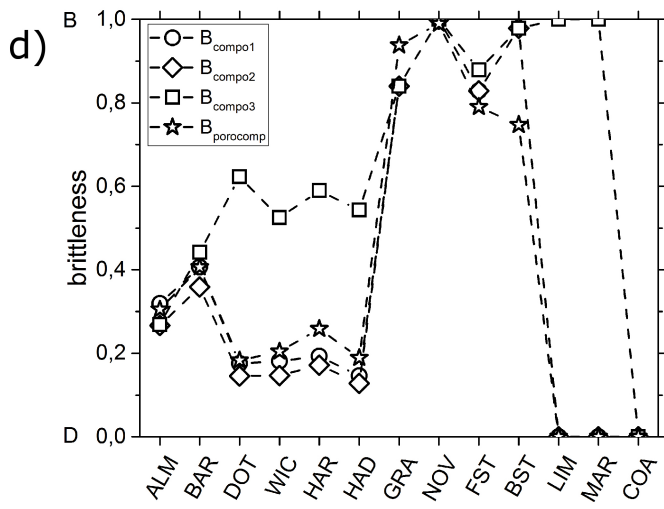
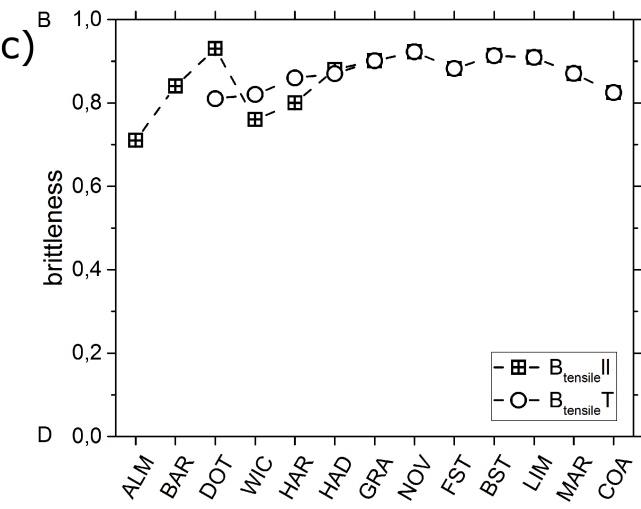
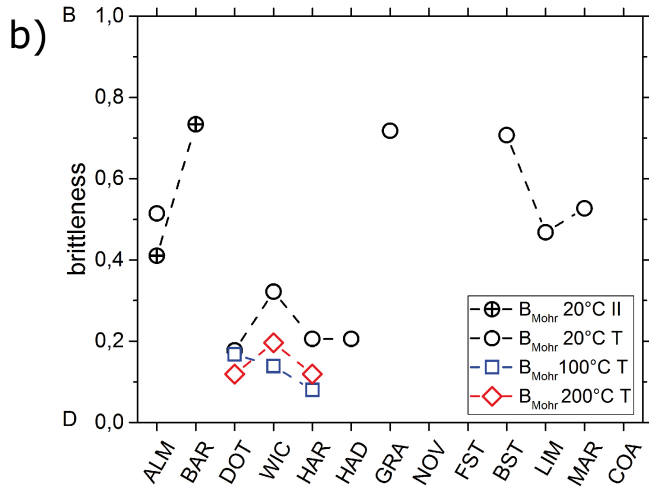
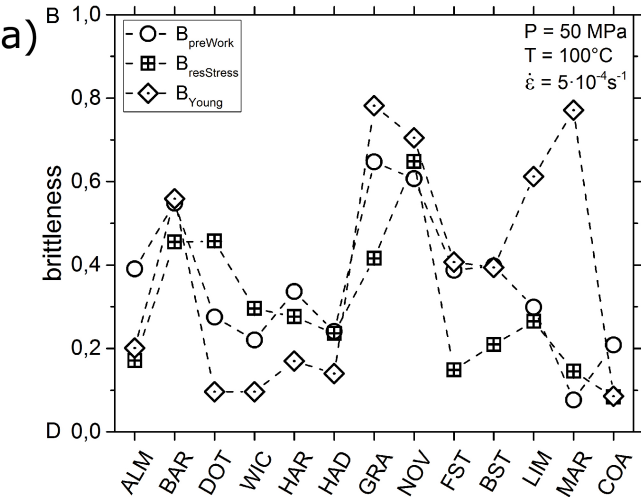


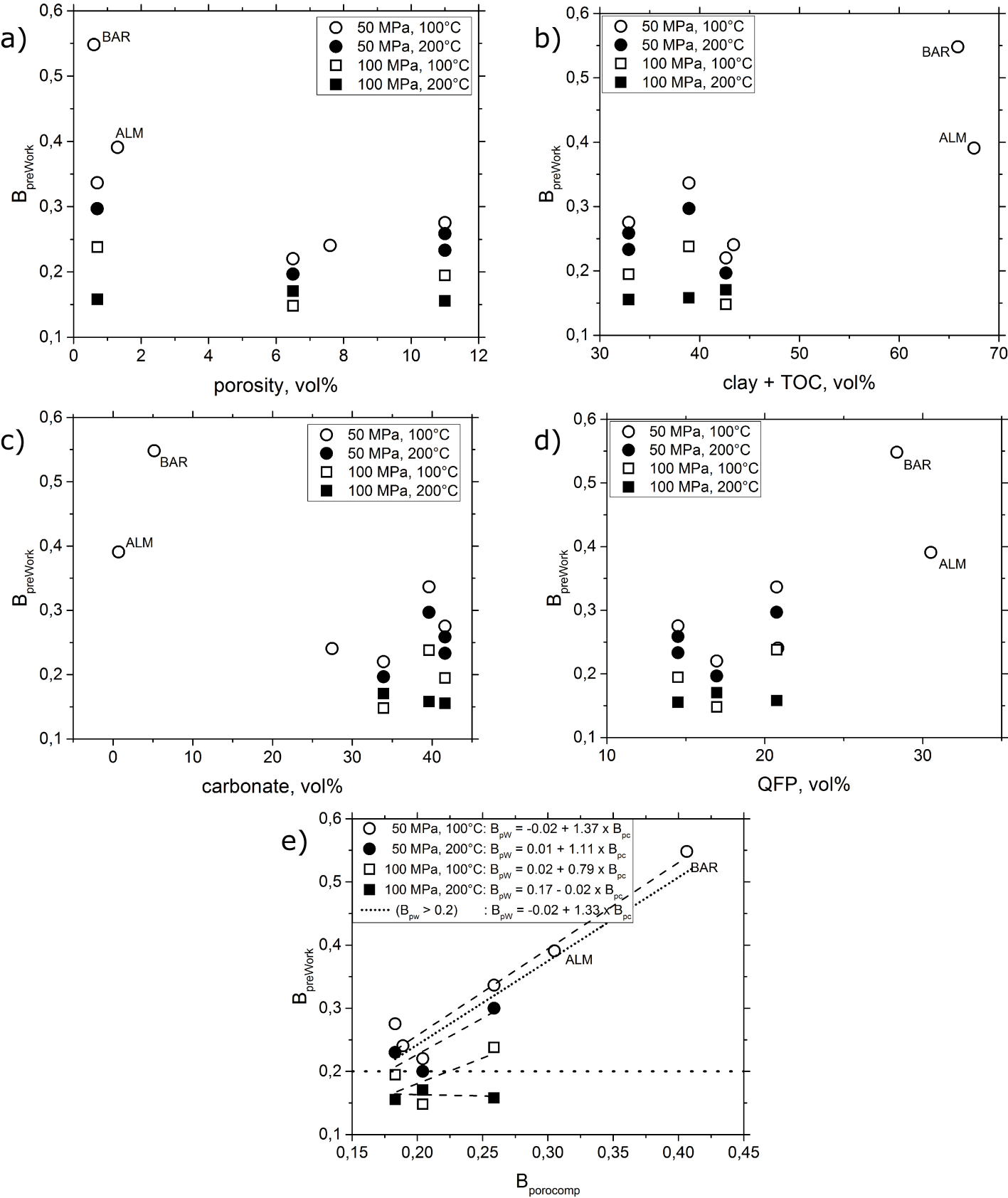












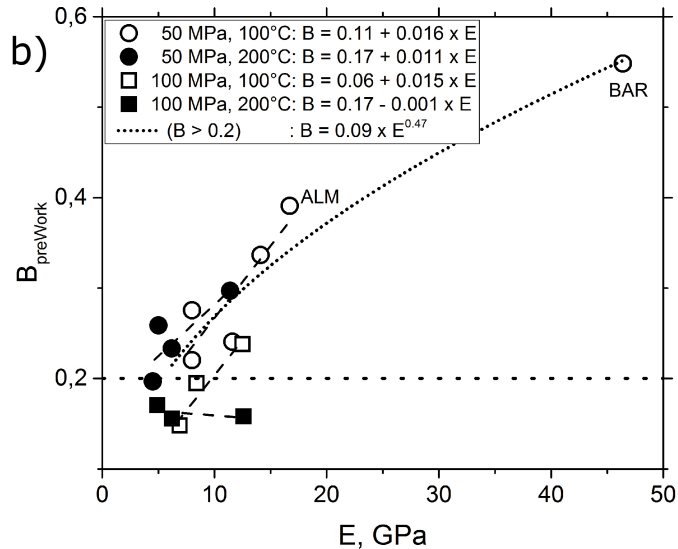
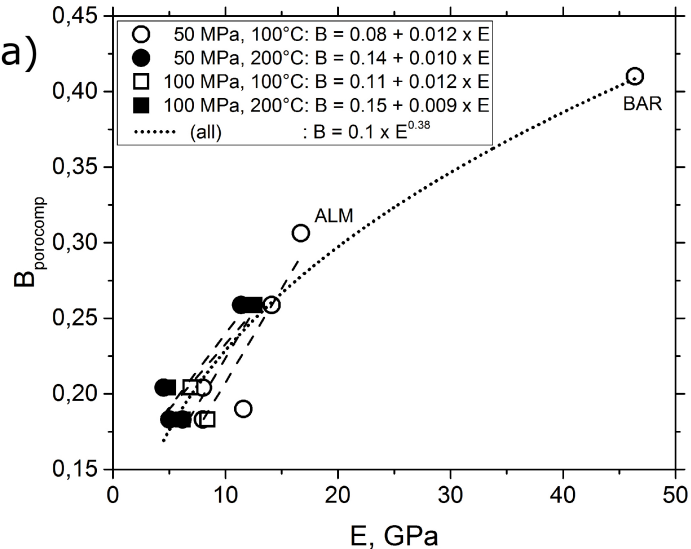


Table 1: Composition of selected samples used in axial compression experiments

Sample	VRr %	Φ vol%	TOC vol%	Cly vol%	Cb vol%	Qtz vol%	Py vol%	Fsp vol%	Px vol%
ALM	3.6	1.3	16.5	51.0	0.7	24.6	3.7	2.1	0
BAR	1.1	0.6	13.8	52.1	5.2	21.5	0.7	6.2	0
DOT	0.6	11	14.9	18.0	41.6	12.7	1.8	0	0
WIC	0.6	6.5	17.0	25.6	33.9	13.2	2.2	1.6	0
HAR	0.9	0.7	10.5	28.4	39.6	16.3	2.4	2.1	0
HAD	1.3	8.3	10.8	32.6	27.5	13.8	2.5	4.5	0
NOV		<1	0	0	0.0	100	0	0	0
FST		9.2	0	9.4	3.9	64.4	0	13.1	0
BST		23.9	0	1.6	0	73	0	1.5	0
LIM		<1	0	0	100	0	0	0.0	0
MAR		<1	0	0	100	0	0	0.0	0
COA		<1	100	0	0	0	0	0.0	0
GRA		<1	0	5.3	0	27.8	0	66.9	0
GAB		<1	0	0	0	0	5.8	67.5	26.6

Table 2: Brittleness index values

brittleness	ALM	BAR	DOT	WIC	HAR	HAD	GRA	NOV	FST	BST	LIM	MAR	COA
B _{compo1}	0.32	0.41	0.18	0.18	0.19	0.15	0.84	1.00	0.83	0.98	0.00	0.00	
B _{compo2}	0.27	0.36	0.15	0.15	0.17	0.13	0.84	1.00	0.83	0.98	0.00	0.00	0.00
B _{compo3}	0.27	0.44	0.62	0.52	0.59	0.54	0.84	1.00	0.88	0.98	1.00	1.00	0.00
B _{compo4}	0.26	0.47	0.61	0.52	0.58	0.54	0.95	1.00	0.90	0.98	1.00	1.00	0.00
B _{porocomp} (wCb = 0.5)	0.31	0.41	0.18	0.20	0.26	0.19	0.94	0.99	0.79	0.75	0.00	0.00	0.00
B _{porocompo} (wQFP = wCb = 0.5)	0.18	0.26	0.10	0.11	0.15	0.10	0.88	0.98	0.65	0.60	0.00	0.00	0.00
B _{tensile}			0.81	0.82	0.86	0.87	0.90	0.92	0.88	0.91	0.91	0.87	0.82
B _{tensile} *	0.71	0.84	0.93	0.76	0.80	0.88	0.90	0.92	0.88	0.91	0.91	0.87	0.82
B _{Mohr} 20°C	0.51		0.18	0.32	0.21	0.21	0.72			0.71	0.47	0.53	0.29
B _{Mohr} 100°C			0.17	0.14	0.08								
B _{Mohr} 200°C			0.12	0.20	0.12								
B _{Mohr} * 20°C	0.41	0.73					0.72			0.71	0.47	0.53	0.29
B _{preWork} 0.1MPa, 20°C	0.89	0.86	0.73	0.88	0.99	0.76							
B _{preWork} 50MPa, 20°C			0.25	0.29	0.36	0.28							
B _{preWork} 100MPa, 20°C			0.22	0.25	0.43	0.22							
B _{preWork} 50MPa, 100°C	0.39	0.55	0.28	0.22	0.34	0.24	0.65	0.61	<i>0.39</i>	0.40	0.30	<i>0.08</i>	<i>0.21</i>
B _{preWork} 100MPa, 100°C			<i>0.19</i>	<i>0.15</i>	0.24								
B _{preWork} 50MPa, 200°C			0.23	<i>0.20</i>	0.30								
B _{preWork} 100MPa, 200°C			<i>0.16</i>	<i>0.17</i>	<i>0.16</i>								
B _{preStrain} 0.1MPa, 20°C	0.99	0.99	0.82	0.83	0.91	0.84							
B _{preStrain} 50MPa, 20°C			0.38	0.42	0.50	0.41							
B _{preStrain} 100MPa, 20°C			0.34	0.38	0.57	0.34							
B _{preStrain} 50MPa, 100°C	0.53	0.67	0.41	0.34	0.48	0.37	0.76	1.00	<i>0.54</i>	0.56	0.44	<i>0.06</i>	<i>0.32</i>
B _{preStrain} 100MPa, 100°C			<i>0.31</i>	<i>0.24</i>	0.37								
B _{preStrain} 50MPa, 200°C			0.36	<i>0.31</i>	0.43								
B _{preStrain} 100MPa, 200°C			<i>0.25</i>	<i>0.28</i>	<i>0.26</i>								
B _{preHarden} 0.1MPa, 20°C	0.91	0.92	0.52	0.55	0.85	0.84							
B _{preHarden} 50MPa, 20°C			0.13	0.16	0.22	0.16							
B _{preHarden} 100MPa, 20°C			0.12	0.13	0.18	0.12							
B _{preHarden} 50MPa, 100°C	0.26	0.41	0.14	0.13	0.20	0.14	0.38	1.00	<i>0.23</i>	0.29	0.12	<i>0.02</i>	<i>0.13</i>
B _{preHarden} 100MPa, 100°C			<i>0.10</i>	<i>0.08</i>	0.13								
B _{preHarden} 50MPa, 200°C			0.12	<i>0.11</i>	0.17								
B _{preHarden} 100MPa, 200°C			<i>0.09</i>	<i>0.09</i>	<i>0.08</i>								
B _{resStress} 0.1MPa, 20°C	0.08	0.20	0.08	0.12	0.79	0.03							
B _{resStress} 50MPa, 20°C			0.43	0.35	0.34	0.22							
B _{resStress} 100MPa, 20°C			0.19	0.09	0.20	0.23							
B _{resStress} 50MPa, 100°C	0.17	0.46	0.46	0.30	0.28	0.24	0.42	0.65	<i>0.15</i>	0.21	0.26	<i>0.15</i>	<i>0.08</i>
B _{resStress} 100MPa, 100°C			<i>0.14</i>	<i>0.08</i>	0.14								
B _{resStress} 50MPa, 200°C			0.42	<i>0.27</i>	0.24								
B _{resStress} 100MPa, 200°C			<i>0.11</i>	<i>0.08</i>	<i>0.11</i>								
B _{resStrain} 0.1MPa, 20°C	0.97	0.96	0.99	1.00	0.98	0.98							
B _{resStrain} 50MPa, 20°C			0.32	0.47	0.68	0.70							
B _{resStrain} 100MPa, 20°C			0.36	0.53	0.55	0.30							
B _{resStrain} 50MPa, 100°C	0.69	0.57	0.35	0.58	0.73	0.59	0.85	0.71	<i>0.73</i>	0.63	0.21	<i>0.50</i>	<i>0.52</i>
B _{resStrain} 100MPa, 100°C			<i>0.41</i>	<i>0.52</i>	0.58								
B _{resStrain} 50MPa, 200°C			0.48	<i>0.44</i>	0.69								
B _{resStrain} 100MPa, 200°C			<i>0.52</i>	<i>0.55</i>	<i>0.37</i>								
B _{Young} 0.1MPa, 20°C	0.13	0.14	0.11	0.13	0.18	0.18							
B _{Young} 50MPa, 20°C			0.12	0.10	0.23	0.16							
B _{Young} 100MPa, 20°C			0.10	0.12	0.14	0.13							
B _{Young} 50MPa, 100°C	0.20	0.56	0.10	0.10	0.17	0.14	0.78	0.70	<i>0.41</i>	0.39	0.61	<i>0.77</i>	<i>0.09</i>
B _{Young} 100MPa, 100°C			<i>0.10</i>	<i>0.08</i>	0.15								
B _{Young} 50MPa, 200°C			0.07	<i>0.05</i>	0.14								
B _{Young} 100MPa, 200°C			<i>0.07</i>	<i>0.06</i>	<i>0.15</i>								

Indices were determined normal to bedding, except those denoted with * (= parallel bedding). Values given in italic notation indicate samples that deformed ductile without post-failure weakening.

Table 3: Brittleness index values vs deformation conditions

DOT, 20°C, $5 \times 10^{-4} \text{s}^{-1}$									
pressure, MPa	0.1	50	75	100	150	200	300	400	
$B_{\text{preWork}}^{\text{T}}$	0.73	0.25	0.26	0.22	0.17	0.17	0.16	0.19	
$B_{\text{preStrain}}^{\text{T}}$	0.82	0.38	0.39	0.34	0.28	0.27	0.26	0.29	
$B_{\text{preHarden}}^{\text{T}}$	0.52	0.13	0.13	0.12	0.09	0.10	0.10	0.11	
$B_{\text{resStress}}^{\text{T}}$	0.08	0.43	0.30	0.19	0.09	0.03	0.00	0.00	
$B_{\text{resStrain}}^{\text{T}}$	0.99	0.32	0.31	0.36	0.49	0.63	0.90	1.00	
$B_{\text{Young}}^{\text{T}}$	0.11	0.12	0.10	0.10	0.12	0.11	0.10	0.09	
DOT, 50 MPa, $5 \times 10^{-4} \text{s}^{-1}$									
temperature, °C	20	50	75	100	150	200	200	300	400
$B_{\text{preWork}}^{\text{T}}$	0.25	0.27	0.27	0.28	0.24	0.26	0.23	0.24	0.71
$B_{\text{preStrain}}^{\text{T}}$	0.38	0.41	0.40	0.41	0.37	0.39	0.36	0.36	0.80
$B_{\text{preHarden}}^{\text{T}}$	0.13	0.16	0.16	0.14	0.13	0.12	0.12	0.12	0.52
$B_{\text{resStress}}^{\text{T}}$	0.43	0.44	0.42	0.46	0.40	0.34	0.42	0.40	0.32
$B_{\text{resStrain}}^{\text{T}}$	0.32	0.38	0.38	0.35	0.44	0.46	0.48	0.61	0.96
$B_{\text{Young}}^{\text{T}}$	0.12	0.13	0.14	0.10	0.10	0.06	0.07	0.06	0.01
WIC, 50 MPa, 100°C									
strain rate, s^{-1}	5×10^{-6}	5×10^{-6}	5×10^{-5}	5×10^{-4}	5×10^{-3}				
$B_{\text{preWork}}^{\text{T}}$	0.15	0.16	0.18	0.18	0.30				
$B_{\text{preStrain}}^{\text{T}}$	0.25	0.27	0.28	0.29	0.46				
$B_{\text{preHarden}}^{\text{T}}$	0.09	0.09	0.11	0.10	0.10				
$B_{\text{resStress}}^{\text{T}}$	0.33	0.31	0.11	0.12	0.12				
$B_{\text{resStrain}}^{\text{T}}$	0.66	0.63	0.61	0.62	0.52				
$B_{\text{Young}}^{\text{T}}$	0.09	0.07	0.09	0.09	0.09				
ALM, 50 MPa, 100°C, $5 \times 10^{-4} \text{s}^{-1}$									
H ₂ O, wt%	0 II	3.6 II	3.8 II	3.6 T					
$B_{\text{preWork}}^{\text{T, II}}$	0.39	0.37	0.48	0.39					
$B_{\text{preStrain}}^{\text{T, II}}$	0.51	0.50	0.62	0.53					
$B_{\text{preHarden}}^{\text{T, II}}$	0.30	0.23	0.29	0.26					
$B_{\text{resStress}}^{\text{T, II}}$	0.21	0.22	0.17	0.17					
$B_{\text{resStrain}}^{\text{T, II}}$	0.69	0.75	0.52	0.69					
$B_{\text{Young}}^{\text{T, II}}$	0.42	0.32	0.31	0.20					

T and II denote loading normal and parallel to bedding, respectively.

Table A1: Brittleness index definitions based on composition

Equation	Remarks
$B_{compo} = \frac{F_{sb}}{F_{sb} + F_{wd}} \quad (A1)$ <p>with:</p> <p>1) $F_{sb} = F_{Qtz}$, $F_{wd} = F_{Cb+Cly}$ (Jarvie et al., 2007)</p> <p>2) $F_{sb} = F_{Qtz+Dol}$, $F_{wd} = F_{Cal+Cly+TOC}$ (Wang and Gale, 2009)</p> <p>3) $F_{sb} = F_{Qtz+Cb}$, $F_{wd} = F_{Cly+TOC}$ (Glorioso and Rattia, 2012)</p> <p>4) $F_{sb} = F_{Qtz+Fsp+Mca+Cb}$, $F_{wd} = F_{total} - F_{sb}$ (Jin et al., 2014)</p>	<p>$B = 1$ (brittle) – 0 (ductile), F_{sb} = fraction of strong/brittle minerals (in wt%), F_{wd} = fraction of weak/ductile minerals (in wt%), Qtz = quartz, Fsp = feldspar, Cb = carbonates, Cly = clay, Dol = dolomite, Cal = calcite, Mca = mica, TOC = total organic carbon</p>
$B_{porocomp} = \frac{w_{sb} F_{sb}}{w_{sb} F_{sb} + w_{Cb} F_{Cb} + w_{wd} F_{wd} + w_{\phi} \phi} \quad (A2)$ <p>with:</p> <p>$F_{sb} = F_{QFP}$, $F_{wd} = F_{Cly+TOC}$, $w_{sb} = w_{wd} = w_{\phi} = 1$, $w_{Cb} = 0.5$ (this paper)</p>	<p>$B = 1$ (brittle) – 0 (ductile), F_{sb} = fraction of strong/brittle minerals (in vol%), F_{wd} = fraction of weak/ductile minerals (in vol%), F_{Cb} = fraction of carbonates (in vol%), ϕ = porosity (in vol%), w_{xx} = weighting factor [0 – 1] for fraction xx, QFP = Qtz+Fsp+Py (pyrite)</p>

Table A2: Brittleness index definitions based on deformation behavior

Equation	Remarks
(pre-) failure deformation behavior	
$B_{preStrain} = \frac{\varepsilon_{el}}{\varepsilon_{fail}} = \frac{\varepsilon_{el}}{\varepsilon_{el} + \varepsilon_{inel}} \quad (A3)$ <p style="text-align: right;">(in: Hucka and Das, 1974)</p>	<p>$B = 1$ (brittle) – 0 (ductile), ε_{el} = elastic (reversible) strain, ε_{inel} = inelastic (irreversible) strain, ε_{fail} = total (or peak) strain at failure, - alternatively (not normalized): $B_{ratioStrain} = \varepsilon_{inel} / \varepsilon_{el}$</p>
$B_{preWork} = \frac{W_{el}}{W_{fail}} = \frac{W_{el}}{W_{el} + W_{inel}} \quad (A4)$ <p style="text-align: right;">(in: Andreev, 1995)</p>	<p>$B = 1$ (brittle) – 0 (ductile), W_{el} = elastic (reversible) energy, W_{inel} = inelastic energy, W_{fail} = total (or peak) energy at failure, - alternatively (not normalized): $B_{ratioWork} = W_{inel} / W_{el}$</p>
$B_{preHarden} = \frac{H}{E} = \frac{\sigma_{inel}}{\varepsilon_{inel}} \frac{1}{E} = \frac{\sigma_{fail} - \sigma_{el}}{\varepsilon_{fail} - \varepsilon_{el}} \frac{1}{E} \quad (A5)$ <p style="text-align: right;">(this paper)</p>	<p>$B = 1$ (brittle) – 0 (ductile), σ_{fail} = total (or peak) stress at failure, H = hardening modulus</p>
$B_{iniStrain} = \varepsilon_{ini} / \varepsilon_{fail} \quad (A6)$ <p style="text-align: right;">(this paper)</p>	<p>$B = 1$ (brittle) – 0 (ductile), ε_{ini} = strain at onset of fracture initiation (dilatancy)</p>
$B_{iniWork} = W_{ini} / W_{fail} \quad (A7)$ <p style="text-align: right;">(in: Andreev, 1995)</p>	<p>$B = 1$ (brittle) – 0 (ductile), W_{ini} = energy at onset of fracture initiation (dilatancy)</p>
$B_{Mohr} = \sin(\varphi) = \mu / \sqrt{1 + \mu^2} \quad (A8)$ <p style="text-align: right;">(Hucka and Das, 1974)</p>	<p>brittle: high B φ = angle of internal friction, $\mu = \tan(\varphi)$ = coefficient of internal friction, requires multiple compression tests at different confining pressures σ_3, assumes Mohr-Coulomb failure: $\sigma_1 = \sigma_C + m\sigma_3$ with σ_C = unconfined (uniaxial) compressive strength (UCS) and $m = \left[\sqrt{(\mu^2 + 1)} + \mu \right]^2$</p>
$B_{tensile} = \frac{\sigma_C - \sigma_T}{\sigma_C + \sigma_T} \quad (A9)$ <p style="text-align: right;">(Hucka and Das, 1974)</p>	<p>brittle: $B = 1$ ($\sigma_C \gg \sigma_T$) σ_T = (unconfined) tensile strength, - alternatively (not normalized): $B_{ambientRatio} = \sigma_C / \sigma_T$ (Andreev, 1995)</p>
$B_{UCSt} = (\sigma_C \cdot \sigma_T) / 2 \quad (A10)$ <p style="text-align: right;">(Altindag, 2002)</p>	<p>- alternatively: $B_{SUCSt} = B_{UCSt}^{1/2}$</p>
post-failure deformation behavior	
$B_{resStress} = \frac{\sigma_{fail} - \sigma_{res}}{\sigma_{fail}} \quad (A11)$ <p style="text-align: right;">(Smolczyk and Gartung 1979)</p>	<p>$B = 1$ (brittle) – 0 (ductile), σ_{res} = residual (friction) strength, - alternatively (brittle: $B = 0$): $B_{resStressRatio} = \sigma_{res} / \sigma_{fail}$ (in Andreev, 1995)</p>

$B_{degree} = \frac{\sigma_{fail} - \sigma_{res}}{\sigma_{fail}} \frac{1}{10} \log \left \frac{\sigma_y - \sigma_{res}}{\varepsilon_y - \varepsilon_{res}} \right \quad (A12)$ <p style="text-align: right;">(Meng et al., 2014)</p>	<p>$B = 1$ (brittle) – 0 (ductile), σ_y, ε_y = yield stress, strain, ε_{res} = residual strain, - alternatively (not normalized):</p> $B_{intens} = (\sigma_{fail} - \sigma_{res}) \frac{1}{10} \log \left \frac{\sigma_{fail} - \sigma_{res}}{\varepsilon_{fail} - \varepsilon_{res}} \right $ <p style="text-align: right;">(Meng et al., 2014)</p>
$B_{resStrain} = \frac{\varepsilon_{res} - \varepsilon_{fail}}{\varepsilon_{res}} \quad (A13)$ <p style="text-align: right;">(modified from Andreev, 1995)</p>	<p>$B = 0$ (brittle) – 1 (ductile), - alternatively (brittle: $B = 1$):</p> $B_{resStrainRatio} = \frac{\varepsilon_{fail}}{\varepsilon_{res}}$
$B_{pfl} = (\varepsilon_{plf} - \varepsilon_{plpf}) / \varepsilon_{plpf} \quad (A14)$ <p style="text-align: right;">(Hajiabdolmajid and Kaiser, 2003)</p>	<p>brittle: high B, ε_{plf} = plastic strain level for breaking of bonds between grains, ε_{plpf} = plastic strain level for shearing of new surfaces</p>
$B_{resME} = \frac{M}{E + M} \quad (A15)$ <p style="text-align: right;">(Andreev, 1995)</p>	<p>brittle: $B = -\infty$ (Class I), $B > 0.5$ (Class II), ductile: $B = 0$ M = descendant (weakening) modulus, $M < 0$ for Class I, $M > 0$ for Class II rocks, - alternatively:</p> $B_{resMR} = M / E$
$B_{resEM} = \frac{M - E}{M} \quad (A16)$ <p style="text-align: right;">(Tarasov and Potvin, 2013)</p>	<p>brittle: $B = 1$ (Class I), $B = 0$ (Class II), ductile: $B = +\infty$ - alternatively:</p> $B_{resHM} = \frac{M - H}{M}$ <p style="text-align: center;">- or:</p> $B_{resER} = E / M$

Table A3: Brittleness index definitions based on elastic properties

Equation	Remarks
$B_{elastic} = \frac{1}{2} \left(\frac{E - E_{min}}{E_{max} - E_{min}} + \frac{\nu - \nu_{max}}{\nu_{min} - \nu_{max}} \right) 100 \quad (A17)$ <p>with:</p> <p>1) $E_{max} = 10$ Mpsi (≈ 69 GPa), $\nu_{min} = 0$, $E_{min} = 0$ Mpsi, $\nu_{max} = 0.5$ (Grieser and Bray, 2007)</p> <p>2) $E_{max} = 8$ Mpsi (≈ 55 GPa), $\nu_{min} = 0.15$, $E_{min} = 1$ Mpsi (≈ 7 GPa), $\nu_{max} = 0.4$ (Rickman et al., 2008)</p>	<p>brittle: high B (in %), i.e., high E, low ν, E = static Young's modulus, ν = static Poisson's ratio, assumed relation between static and dynamic properties (Mullen et al., 2007): $\nu_{stat} = \nu_{dyn}$, E_{stat} [Mpsi] = $E_{dyn} \cdot (0.8 - \Phi)$, Φ = total porosity, - alternatively (simplified):</p> $B_{Young} = \frac{E - E_{min}}{E_{max} - E_{min}}$
$B_{Lame} = \frac{\lambda + 2G}{\lambda} \quad (A18)$ <p>(Guo et al., 2012)</p>	<p>brittle: high B, λ = 1st Lamé parameter (incompressibility), G = 2nd Lamé parameter (rigidity = shear modulus), $\lambda = (E\nu) / [(1 + \nu)(1 - 2\nu)]$, $G = E / [2(1 + \nu)]$</p>
$B_{Yd} = E \cdot \rho \quad (A19)$ <p>(Sharma and Chopra, 2012)</p>	<p>brittle: high B, ρ = density</p>
$B_{Yi} = E / \lambda \quad (A20)$ <p>(Chen et al., 2014)</p>	<p>brittle: high B</p>
$B_{bi} = (3K - 5\lambda) / \lambda \quad (A21)$ <p>(Huang et al., 2015)</p>	<p>brittle: high B, K = bulk modulus</p>

Table A4: Brittleness index definitions based on indentation characteristics

Equation	Remarks
$B_{punch} = \frac{F_{max}}{P_x} \quad (A22)$ <p style="text-align: right;">(Yagiz, 2009)</p>	brittle: $B > 40$ kN/mm, ductile: $B < 19$ kN/mm P_x = penetration depth (in mm) at maximum applied force F_{max} (in kN)
$B_{fines} = q \cdot \sigma_t \quad (A23)$ <p style="text-align: right;">(Hucka and Das, 1974)</p>	q = percentage of fines (below 28 mesh) obtained from Protodyakonov's impact test
$B_{forcestep} = \frac{P_{dec}}{P_{inc}} \quad (A24)$ <p style="text-align: right;">(Copur et al., 2003)</p>	P_{dec} = average force decrement period, P_{inc} = average force increment period during indentation testing
$B_{VickLength} = \frac{C}{a} \quad (A25)$ <p style="text-align: right;">(Sehgal et al., 1995)</p>	C = characteristic crack length, a = indentation diagonal length for Vicker's indentation testing in glass
$B_{indent} = \frac{H_\mu - H_m}{c} \quad (A26)$ <p style="text-align: right;">(Hucka and Das, 1974)</p>	H_μ = micro-indentation hardness, H_m = macro-indentation hardness, $c = 2.6$ for Vicker's hardness testing
$B_{tough} = \frac{H_a}{K_c} \quad (A27)$ <p style="text-align: right;">(Lawn and Marshall, 1979)</p>	H_a = hardness (resistance to deformation, in GPa), K_c = fracture toughness (resistance to fracture propagation, in MPam ^{1/2}) or $B_{toughS} = \left(\frac{H_a}{K_c}\right)^2$ (Lawn et al., 1976)
$B_{toughE} = \frac{H_a \cdot E}{K_c^2} \quad (A28)$ <p style="text-align: right;">(Quinn and Quinn, 1997)</p>	ratio of deformation (indentation) work per unit volume to fracture surface energy per unit area

Table A5: Brittleness index definitions based on miscellaneous properties

Equation	Remarks
$B_{disk} = \frac{h}{d} \quad (A29)$ <p style="text-align: right;">(Andreev, 1995)</p>	brittle: $B < 1/3$, core disk with: h = core disk thickness, d = core diameter
$B_{crush} = W/\sigma_t \quad (A30)$ <p style="text-align: right;">(Andreev, 1995)</p>	brittle: high B , W = work consumed for crushing a rock
$B_{OCNC} = \frac{\sigma_c}{\sigma_{c-NC}} \quad (A31)$ <p style="text-align: right;">(Ingram and Urai, 1999)</p>	brittle: $B > 2$, σ_{c-NC} = UCS of a normally consolidated rock in non-overpressured areas, $\sigma_{c-NC} \approx 0.5\sigma_{eff}$, with σ_{eff} = effective in-situ stress corresponding to normal consolidation at the depth of interest
$B_{OCR} = OCR^b \quad (A32)$ <p style="text-align: right;">(Nygard et al, 2006)</p>	brittle: $OCR > 2.5$, $OCR = \sigma_{maxH}/\sigma_{act}$ = overconsolidation ratio, $\sigma_{maxH} \approx 8.6 \cdot \sigma_c^{0.55}$ = max. effective stress that a rock was subjected to in history, σ_{act} = current effective stress, $b \approx 0.89$,
$B_{total} = \frac{B_{elastic} + B_{compo}}{2} \quad (A33)$ <p style="text-align: right;">(Guo et al., 2015)</p>	brittle: B high, ‘total’ brittleness
$F_{norm} = \frac{B_n + X_n}{2} \quad (A34)$ <p style="text-align: right;">(Jin et al., 2014)</p> <p>with: 1) $X = G_c$, 2) $X = K_{Ic}$, 3) $X = E$ using normalized parameters (index n): $B_n = \frac{B - B_{min}}{B_{max} - B_{min}},$ $X_n = \frac{X_{max} - X}{X_{max} - X_{min}}$ </p>	best fracable: $F = 1$, worst fracable: $F = 0$, F = fracability, K_{Ic} = Mode I (tensile) fracture toughness, $G_c = K_{Ic}^2/E$ = critical energy release rate, B = brittleness or: $F_{normw} = wB_n + (1-w)X_n$ with w = weight fraction (Jin et al., 2015)
$F_{totalKc} = \frac{2B_{total}}{K_{Ic} K_{IIc}} \quad (A35)$ <p style="text-align: right;">(Yuan et al., 2013, cited in Guo et al., 2015)</p>	F = fracability, K_{IIc} = Mode II (shear) fracture toughness
$F_{totalIF} = \frac{B_{total}}{\sin(\varphi) K_{Ic}} \quad (A36)$ <p style="text-align: right;">(Guo et al., 2015)</p>	F = fracability, φ = angle of internal friction,